Bioactive Materials 38 (2024) 438–454

Contents lists available at ScienceDirect

Bioactive Materials

journal homepage: www.keaipublishing.com/en/journals/bioactive-materials

ROS-responsive nanoparticle delivery of ferroptosis inhibitor prodrug to facilitate mesenchymal stem cell-mediated spinal cord injury repair

Renshuai Hua [a,1], Chenxi Zhao [b,1], Zhengyu Xu [a,1], Derong Liu [a], Wenyuan Shen [a,c], Wenlu Yuan [a], Yan Li [a], Jun Ma [a], Zhishuo Wang [a,**], Shiqing Feng [a,b,c,*]

[a] Department of Orthopedics, International Science and Technology Cooperation Base of Spinal Cord Injury, Tianjin Key Laboratory of Spine and Spinal Cord Injury, Tianjin Medical University General Hospital, 154 Anshan Road, Heping District, Tianjin, 300052, China
[b] Department of Orthopaedics, Qilu Hospital of Shandong University, Shandong University Centre for Orthopaedics, Advanced Medical Research Institute, Cheeloo College of Medicine, Shandong University, Jinan, Shandong, 250012, China
[c] Department of Orthopedics, The Second Hospital of Shandong University, Cheeloo College of Medicine, Shandong University, 247 Beiyuan Street, Jinan, Shandong, 250033, China

ARTICLE INFO

Keywords:
Spinal cord injury
Huc-MSCs
ROS-Responsive nanoparticles
Ferroptosis inhibitor

ABSTRACT

Spinal cord injury (SCI) is a traumatic condition that results in impaired motor and sensory function. Ferroptosis is one of the main causes of neural cell death and loss of neurological function in the spinal cord, and ferroptosis inhibitors are effective in reducing inflammation and repairing SCI. Although human umbilical cord mesenchymal stem cells (Huc-MSCs) can ameliorate inflammatory microenvironments and promote neural regeneration in SCI, their efficacy is greatly limited by the local microenvironment after SCI. Therefore, in this study, we constructed a drug-release nanoparticle system with synergistic Huc-MSCs and ferroptosis inhibitor, in which we anchored Huc-MSCs by a Tz-A6 peptide based on the CD44-targeting sequence, and combined with the reactive oxygen species (ROS)-responsive drug nanocarrier mPEG-b-Lys-BECI-TCO at the other end for SCI repair. Meanwhile, we also modified the classic ferroptosis inhibitor Ferrostatin-1 (Fer-1) and synthesized a new prodrug Feborastatin-1 (Feb-1). The results showed that this treatment regimen significantly inhibited the ferroptosis and inflammatory response after SCI, and promoted the recovery of neurological function in rats with SCI. This study developed a combination therapy for the treatment of SCI and also provides a new strategy for the construction of a drug-coordinated cell therapy system.

1. Introduction

Spinal cord injury (SCI) represents a profound neurological catastrophe. As the global population ages, the prevalence of non-communicable nervous system diseases threatens to climb further, thereby intensifying the already considerable burden on families and society [1]. Current clinical treatment modalities for SCI include surgical decompression and intravenous high-dose methylprednisolone, but they still do not affect the course of the disease and clinical outcomes [2,3]. Although many methods, including novel drugs, cell and exosome transplantation, bioactive scaffolds, etc., have shown good efficacy in preclinical studies, few have reached the progress to clinical trials [4]. Due to the complex pathological process of SCI, a single treatment method often cannot achieve the desired curative effect, and the combination of multiple methods has become a trend in the treatment of SCI [5–7].

Mesenchymal stem cells (MSCs) possess remarkable neural repair capabilities. Studies have shown that transplanted MSCs exhibit neuroprotective function and can increase the proportion of intact tissue in SCI [8–10]. Over the years, many different types of nanomedicines,

Peer review under responsibility of KeAi Communications Co., Ltd.
* Corresponding author. Tianjin Medical University General Hospital, 154 Anshan Road, Heping District, Tianjin, 300052, China.
** Corresponding author. Tianjin Medical University General Hospital, 154 Anshan Road, Heping District, Tianjin, 300052, China.
E-mail addresses: renshuai.hua@outlook.com (R. Hua), doc_zhao07@163.com (C. Zhao), dafu_dagui@163.com (Z. Xu), xiaoliu19971106@163.com (D. Liu), shenwenyuan66@126.com (W. Shen), lunayuan8029@163.com (W. Yuan), lala187218@163.com (Y. Li), 1651789377@qq.com (J. Ma), fengshuiling@hotmail.com (Z. Wang), sqfeng@tmu.edu.cn (S. Feng).
[1] Renshuai Hua, Chenxi Zhao, Zhengyu Xu contributed equally to this work.

https://doi.org/10.1016/j.bioactmat.2024.05.015
Received 10 March 2024; Received in revised form 5 May 2024; Accepted 7 May 2024

including liposomes, polymers, micelles, and antibodies, have been developed for advanced cell therapies, and there has been substantial evidence that these submicron-sized carrier materials can improve the balance between efficacy and toxicity of therapeutic interventions [11–15]. Although some progress has been made with nanomedicine carriers, there are still shortcomings, such as a lack of inherent targeting and rapid clearance by immune cells [16,17]. Due to the inherent properties of MSCs such as low immunogenicity and homing ability, MSCs show great potential for nanoparticle-based drug delivery [18,19]. Hence, the combination strategy of MSCs, nano-biomaterials, and effective drugs may be the key to achieving SCI repair [20–23].

When SCI occurs, the overproduction of reactive oxygen species (ROS) leads to depletion of endogenous antioxidants and disruption of redox homeostasis, which can lead to ferroptosis, and exacerbate the inflammatory response [24,25]. Emerging evidence indicates that ferroptosis is a distinct form of oxidative cell death that plays an essential role in pathogenesis in SCI [26,27]. Ferrostatin-1 possesses the capacity to eliminate hydrogen peroxide free radicals, thereby mitigating cell demise through the suppression of ferroptosis [28,29]. Nevertheless, the low serum stability of Ferrostatin-1 has hindered its promotion in vivo experiments, presenting a pressing issue in its current application [30]. Recent investigations have indicated that nano-encapsulated anti--ferroptosis drug possesses the capacity to eliminate hydrogen peroxide free radicals, thereby mitigating cell demise through the suppression of ferroptosis during SCI [31,32]. Therefore, the exploration of novel, safe anti-ferroptosis drugs and drug-affinity nano-delivery system candidates targeting spinal cord injury is imperative.

Here, we have constructed ROS-responsive nanoparticles and chemically modified the classic anti-ferroptosis drug Ferrostatin-1(Fer-1) to synthesize its prodrug and name it Feborastatin-1(Feb-1). In addition, to develop a solution for nanoparticle loading onto Huc-MSCs, we designed and synthesized a Tz-A6 peptide based on a CD44-targeting sequence. The Tz-A6 peptide can bind to CD44 which is on the surface of Huc-MSCs via the A6 peptide end, and bind to TCO which is in the ROS-responsive drug nanocarrier mPEG-b-Lys-BECI-TCO via the Tz end. In vivo and in vitro studies revealed that Feb-1 could achieve anti-ferroptosis by enhancing GPX-4 and xCT signaling pathways and contribute to functional recovery in rats with SCI. Notably, the combination of Feb-1, MSCs, and NPs promotes the repair and functional recovery of rats with spinal cord injury, leading to beneficial therapeutic effects.

2. Materials and methods

2.1. Synthesis and characterization of amphiphilic copolymers mPEG-b-Lys-BECI-TCO

Poly (ethylene glycol)-b-poly(L-Lysine) (mPEG45-b-PLys20) and 4-(4,4,5,5-tetramethyl-1,3,2-dioxaborolan-2-yl)benzyl-imidazole-carboxylate (HPBA-pinacol) were all prepared as described previously [33]. The detailed synthetic routes for the polymers used in this step are noted separately (Fig. S1). The mPEG45-b-PLys20 was characterized using ^{1}H NMR (D_2O as the internal reference, D_2O: $\delta = 4.79$ ppm). The degree of polymerization (DP) of poly-lysine was estimated to be 20, which was calculated by the peak integration ratio of protons at -CH2CH2O- group of PEG at 3.62–3.84 ppm and -NHCHCO- protons of poly-lysine at 4.15–4.52 ppm (Fig. S2). Then, Poly (ethylene glycol)-b-poly(L-Lysine)-HPBA-pinacol (mPEG-b-Lys-BECI) was prepared as described previously by conjugating the HPBA-pinacol as substrates onto the mPEG45-b-PLys20 mentioned above. Briefly, 40 mg of mPEG45-b-PLys20 (0.01 mmol) was first dissolved in 4 mL chloroform to reach a concentration of 10 mg/mL. Meanwhile, 33 mg HPBA-pinacol (0.1 mmol, 1.0 equivalents to amino groups of the polymer mPEG45-b-PLys20) was dissolved in anhydrous CH_3CN to get a 33 mg/mL stock solution and then added drop wisely into the mixture solutions. At the same time, the pH of the solution was maintained at a strong base by adding 10 μL of N,N-Diisopropylethylamine (DIPEA). After the reaction, unreacted HPBA-pinacol was removed by dialysis (MWCO = 1000 Da), and mPEG-b-Lys-BECI was obtained by lyophilization without further purification. The desired product was confirmed using 1H NMR analysis (Fig. S3), indicating that more than 90 % of the amino groups have been reacted with HPBA-pinacol. mPEG-b-Lys-BECI: ^{1}H NMR (400 MHz, d-DMSO, δ): 7.63 (s, 1H), 7.29 (s, 1H), 4.98 (s, 1H phCH1O), 3.58–3.43 (s, 4H, OCH2CH2O), 3.0–2.9 (s, 1H, NHCH1CO), 2.90 (s, 2H), 2.73 (s, 2H), 1.42–1.20 (m, 8H).

For the synthesis of polyethylene glycol-b-poly(L-lysine)-HPBA-pinacol-trans-cyclooctene, named (mPEG-b-Lys-BECI-TCO). Briefly, 2.67 mg (0.01 mmol, 2 eq.) of (E)-cyclooct-4-enyl (2,5-dioxopyrrolidinyl) carbonate (TCO carbonate) was first dissolved in 500 μL anhydrous tetrahydrofuran (THF) and activated by 1.3 mg (0.01 mmol, 2 eq.) DIPEA. The resulting solution was purged with nitrogen for 20 min and stirred for an additional 10 min in a dry Schlenk tube at room temperature. Subsequently, 30 mg (5 μmol, 1 eq.) of mPEG-b-Lys-BECI was added under N_2 atmosphere. The mixture was diluted with 0.8 mL THF and then stirred at room temperature overnight. After precipitating using cold diethyl ether, unreacted TCO carbonate was removed, and the desired product was re-dissolved in solution (THF: H_2O = 3: 7) and purified by filtering through a 0.45 μm PTFE filter. mPEG-b-Lys-BECI-TCO was obtained by lyophilization, and the TCO group was confirmed using ^{1}H NMR analysis (Fig. S4), indicating that not only the remaining 10 % of free amino groups but also 20 % NH_2 of lysine which were HPBA-pinacol protected are also substituted by TCO group. ^{1}H NMR (400 MHz, d-DMSO, δ): 7.2–6.67 (m, 1H), 5.08–4.89 (m, 0.4 H 1H of ethylene at TCO), 4.99 (s, 0.43 H phCH1O), 4.18 (s, 0.48H), 3.80 (s, 0.16H 1H of 1H C–O at TCO), 3.50 (s, 4H), 3.02–2.78 (m, 1H), 2.32–2.10 (m, 1H), 1.95–1.18 (m, 6H).

2.2. Preparation and characterization of ROS-responsive nanoparticles

For the preparation of Feb-1 encapsulated micelles, mPEG-b-Lys-BECI-TCO (MW = 6000 Da) was used as nanocarriers to prepare ROS Nano@Feb-1. Briefly, 6.0 mg of mPEG-b-Lys-BECI-TCO (0.001 mmol 1eq.) and 1.0 mg Feb-1 (2.5 μmol 2.5 eq.) were dissolved and stirred in 1.0 mL of anhydrous THF. The solution was poured into 10 mL of distilled water and sonicated for 30 min. The mixed solution was centrifuged at 3000 rpm for 10 min. The supernatant was placed into a dialysis bag (MW = 3000 Da) and incubated in DI water or PBS to obtain the desired nanoparticles (ROS Nano@Feb-1). With the various nanoparticles in hand, the size distribution and zeta potential were measured by using Zetasizer Nano (ZS90, Malvern, UK). The nanoparticles were prepared by lyophilization and fixation on a carbon adhesive tape and sputter-coating with an Au layer under vacuum. Immediately thereafter, the micromorphology was observed under a scanning electron microscope (Zeiss, Gemini 300, GER) at a working accelerating voltage of 2 kV.

The loading capacity (LC) and drug encapsulation efficiency EE (%) of Feb-1 in ROS Nano@Feb-1 nanoparticles were determined and calculated by the absorbance peak at 320 nm via UV-VIS spectrum detection. Briefly, the quantitative micelles (M = the mass of the lyophilized NPs) were lyophilized, and redissolved in acetonitrile, fully oscillated and centrifuged at 13000 rpm for 10 min. The supernatant was diluted 4 times with deionized water. The concentration of Feb-1 in the supernatant was determined by a UV-VIS spectrum detector (Thermo Scientific, NanoDrop One^C, USA) following the standard curve method. The LC (%) was calculated according to the formula: LC (%) = $M_0/M \times 100$ %, M_0 is the mass of Feb-1 encapsulated. The drug encapsulation efficiency EE (%) was calculated according to the formula: EE (%) = $M_0/W \times 100$ %, W is the mass of Feb-1 used totally for preparing the NPs. The features of the nanodrug release profile in vitro were characterized by HPLC or UV-VIS spectrum. In order to avoid oxidative of Feb-1 by air at room temperature, the dialysis was performed in a 50 mL centrifuge tube under a nitrogen atmosphere. First,

0.5 mL ROS Nano@Feb-1 was placed into a 10 kDa mini-dialysis tube and incubated in 50 mL water or H_2O_2 (200 μM or 400 μM) solutions. All dialysis media containing 0.5 % sodium dodecyl sulfate (SDS) was placed on a shaker at 37 °C. At predetermined time points, 100 μL of the solution was collected and lyophilized, then the concentration of Feb-1 was detected.

2.3. ROS stimulation promotes ROS Nano@Feb-1 degradation

The features of the nanocarriers under ROS stimulation were characterized and detected as described previously [34]. First, ROS Nano@Feb-1 has dissolved in 1.0 mL H_2O_2 solutions. The concentrations of H_2O_2 were 0, 200, and 400 μM. Then, the nanoparticles were stained with 1 % phosphotungstic acid and the morphological changes of the nanoparticles in the H_2O_2 solution were characterized by transmission electron microscopy (HITACHI, HT7700, JP). At the same time point after oxidation, the size changes were analyzed by dynamic light scattering (DLS).

2.4. Functionalization of A6 peptides with tetrazine as bio-orthogonal handles (Tz-A6 peptide)

The tetrazine crosslinker was synthesized in one step. Details of the routes were provided in the supporting information (Fig. S1a). The solution containing 4-(6-methyl-1,2,4,5-tetrazin-3-yl)phenylmethanamine (methyltetrazine-amine hydrochloride) (24 mg, 0.1 mmol) and DIPEA (2 equiv.) was added dropwise to a mixture of 5.0 mL DCM/methanol (3:1), and then N-succinimidyl-6-maleimidohexanoate (36 mg, 0.12 mmol) was added via syringe under a nitrogen atmosphere. The reaction mixture was mixed totally by sonication and continued to stir at room temperature for 8 h. After evaporation in vacuo, the desired product Mal-tetrazine was purified through a preparative thin layer chromatography. The purification of Mal-tetrazine is carried out at 4 °C using dichloromethane/MeOH (v: v = 100: 5) as a chromatography mobile phase. The product 6-(2,5-dioxo-2,5-dihydro-1H-pyrrol-1-yl)-N-(4-(6-methyl-1,2,4,5-tetrazin-3-yl)benzyl)hexanamide (Mal-tetrazine) was obtained as pink solid (14 mg, 31 % yield). For the preparation of Tz-A6 peptide, A6 peptide (10 mg, 10.2 μmol, 1.0 eq.) was added to the solution of Mal-tetrazine (15 μmol, 6.0 mg, 1.5 equiv.) in DMF (5.0 mL), followed by addition of 1.0 μL DIPEA, and the reaction proceeded at 37 °C for 20 h under constant stirring. All operations are performed in a nitrogen atmosphere. Tz-A6 peptide was isolated by precipitation and centrifugal enrichment in cold anhydrous diethyl ether, then the Tz-A6 peptide was lyophilized without further purification. The product purity and molecular structure were confirmed using HRMS and HPLC analysis (Figs. S6–10).

The binding effect of ROS Nano@Feb-1 by the Tz-A6 peptide was further confirmed through the drug-loading capacity detection of Huc-MSCs via HPLC-MS. The Huc-MSCs were cultured in fresh medium containing various concentrations of the Tz-A6 peptide (0 or 1 μM) for 5 min at 37 °C, 5 % CO_2, and 95 % humidity. Then the MSCs were incubated in the medium with ROS Nano@Feb-1 (1 μM) for 15 min. After treatment, the cells were digested with trypsin and collected by centrifugation. The obtained Huc-MSCs cells were lyophilized in tubes and stored at −80 °C until analysis. Before performing LC-MS analysis, the samples were diluted in 100 μL acetonitrile containing Salvianolic acid B (0.1 mg/mL) as internal standard (IS). The samples were vortexed and sonicated for 5 min. The mixture was centrifuged at 13000 rpm for 5 min at 4 °C to remove the precipitation. Then the supernatant was transferred to an HPLC-MS chromatography vial (Thermo Scientific, Vanquish UPLC; Acquity UPLC BEH C18 1.7 μm, 2.1*100 mm column). The quantitative analysis of Feb-1 and its metabolic intermediates was then quantified using an extracted-ion chromatogram (EIC) mass spectrometry (Thermo Scientific, Orbitrap Exploris 480).

2.5. Tz-A6 peptide increased localization and targeting efficacy in vitro

To identify Tz-A6 peptide targeting efficacy in vitro, fluorescent labeling was performed. The process of preparing ROS Nano@DID with DID (Cat#D4019; Uelandy) instead of Feb-1 was similar. For cell imaging studies, 2×10^5 Huc-MSCs were cultured on confocal small dishes for 24 h. The nuclear F-actin was stained by phalloidin-YF488 (Cat#YP0059L; Uelandy) for 20 min, and the nuclear regions were determined by DAPI. Subsequently, a drug concentration of 10 μg/mL of ROS Nano@DID was added. Cells were imaged using an Olympus FV1000.

To identify the effects of concentrations of A6 peptide on cellular endocytosis, we processed a "click-reaction" fluorescence staining in vitro. Briefly, Huc-MSCs were cultured in the medium that contained different concentrations of Tz-A6 peptide (0–10 μM) for 3 min, followed by addition of BDP FL-PEG4-(4E)-TCO (TCO-Bodipy) (1 μM) (Cat#BCT-16; Confluore) for 3 min. Subsequently, the cell imaging was performed using a fluorescence microscope (Leica, DMi8, GER) and flow cytometry (BD, FACSVerse, US).

2.6. Culture and identification of Huc-MSCs

The Huc-MSCs used for the experiment were supplied by Tianjin Changhe Biotechnology Co., Ltd. Huc-MSCs were cultured in MEM medium (Cat#C11095500BT; Gibco-Invitrogen) containing 10 % FBS (Cat#12664025; Gibco-Invitrogen). Surface markers CD73 (Cat#344015, BioLegend), CD90(Cat#328109, BioLegend), CD105 (Cat#323205, BioLegend), CD14(Cat#325603, BioLegend), CD44 (Cat#397517, BioLegend), CD45(Cat#304011, BioLegend), CD34 (Cat#343503, BioLegend) and CD19(Cat#302205, BioLegend) were used for identifying Huc-MSCs by flow cytometry [35]. IgG Fc was used as the corresponding negative control (Fig. S5).

2.7. Synthesis of ethyl 4-(cyclohexylamino)-3-((4-(4,4,5,5-tetramethyl-1,3,2-dioxaborolan-2-yl)benzyl)amino)benzoate (Feb-1)

Prodrug Feb-1 was synthesized in one step via classical base-catalyzed nucleophilic substitution. To synthesize Feb-1, 4-(bromomethyl) benzeneboronic acid pinacol ester (0.2, 0.7 mmol, 1.0 eq.) was dissolved in 5.0 mL dichloromethane. Then, ferrostatin-1 (367.29 mg, 1.4 mmol, 2 eq.) was quickly dissolved in 1.0 mL methanol, followed by the addition of N, N-diisopropylethylamine as an alkaline catalyst (235 mg, 2.5 eq.). This mixture was allowed to stir at room temperature for 18 h. After concentration, the residue was further purified by prepacked silica column chromatography to remove the byproduct. The eluent used was a mixture of ethyl acetate/hexane = 1/5 (v/v). Then, the crude product was purified by normal phase chromatography and further lyophilized to yield compound Feb-1 as a white solid. (100.6 mg, 30 % yield). 1H NMR (CDCl3, 400 MHz): δ (ppm) 7.82 (d, J = 8.0 Hz, 2H), 7.60 (d, J = 8.4 Hz, 1H), 7.470–7.38 (m, 3H), 6.62 (d, J = 8.4 Hz, 1H), 4.35–4.26 (m, 4H), 4.20–4.03 (m, 1H), 3.36–3.28 (m, 1H), 2.11–1.99 (m, 3H), 1.47–1.26 (m, 23H). 13C NMR (CDCl3, 100 MHz): δ (ppm) 167.4, 142.6, 142.2, 141.7, 135.3, 134.9, 127.7, 123.9, 119.1, 115.1, 109.6, 84.0, 60.3, 51.6, 49.8, 33.5, 26.03, 25.07, 25.02, 14.62. HRMS-ESI+: calculated for C28H40BN2O4+, 479.3076; found 479.3087 (Fig. S12).

2.8. Cell viability assay

The effects of Feb-1 and Fer-1 on the cell viability of Huc-MSCs were identified using CCK-8 (Cat# CK04, Dojindo). Following the removal of the original medium, fresh medium containing appropriate concentrations of 0.1 % DMSO solution in PBS or Fer-1 (0.1 μM, 1 μM, 10 μM, 100 μM) or Feb-1 (0.1 μM, 1 μM, 10 μM, 100 μM) was added. The cells were then incubated at 37 °C for 24 h. Following the addition of CCK-8, the samples were incubated in a 37 °C incubator for 2 h, and then the

absorbance was measured using a microplate reader. The plates were placed in a microplate reader (ELx800; Bio-Tek) to detect the absorbance at 450 nm.

To assess the cytotoxicity of RSL3 (Cat# S8155; Selleck) on Huc-MSCs, we cultured the cells in fresh medium containing various concentrations of RSL3 (0–8 μM) for 24 h at 37 °C, 5 % CO_2, and 95 % humidity. After 24 h of incubation in the medium with RSL3, CCK-8 (Cat# CK04, Dojindo) was added. Following the addition of CCK-8, the samples were incubated in a 37 °C incubator, and then the absorbance was measured using a microplate reader to detect the absorbance at 450 nm.

A concentration of 6 μM RSL3 was used to induce ferroptosis in Huc-MSCs. Following the removal of the original medium, fresh medium containing appropriate concentrations of 0.1 % DMSO solution in PBS or RSL3 (6 μM) or RSL3 (6 μM) + Fer-1 (1 μM) or RSL3 (6 μM) + Feb-1 (1 μM) was added. The cells were then incubated at 37 °C for 24 h. Subsequently, the medium was removed and incubation was continued for 2 h with the addition of CCK-8. The absorbance was then measured at 450 nm using a microplate reader.

In experiments on the restorative effects of different concentrations of Fer-1 and Feb-1 on H_2O_2-induced death of Huc-MSCs, 200 μM H_2O_2 was used as the inducing condition. Following the removal of the original medium, fresh medium containing appropriate concentrations of 0.1 % DMSO solution in PBS or H_2O_2 (200 μM) or H_2O_2 (200 μM) + Fer-1 (1 nM, 10 nM, 100 nM, 1000 nM) or H_2O_2 (200 μM) + Feb-1 (1 nM, 10 nM, 100 nM, 1000 nM) was added. The cells were then incubated at 37 °C for 2 h. After incubation, the medium was removed and CCK-8 was added to continue incubation at 37 °C for 2 h. The absorbance was then measured at 450 nm using a microplate reader.

In the experiment to detect the efficacy of ROS Nano@Feb-1, 6 μM RSL3 was used to induce ferroptosis in Huc-MSCs. Following the removal of the original medium, a fresh medium containing PBS or RSL3 (6 μM) or RSL3 (6 μM) + ROS Nano@Feb-1 (Feb-1 concentrations of approximately 1 nM, 10 nM) was added. In the experiment to test the efficacy of ROS Nano@Feb-1 with Tz-A6 peptide, cells were incubated with a medium containing 1 μM Tz-A6 peptide for 5 min. After washing with PBS buffer, a fresh medium containing PBS or RSL3 (6 μM) or RSL3 (6 μM) + ROS Nano@Feb-1 (Feb-1 concentrations of approximately 0.01 nM, 0.1 nM, 1 nM, 10 nM) was added. The cells were then incubated at 37 °C for 24 h. After incubation, the medium was removed and CCK-8 was added to continue incubation at 37 °C for 2 h. The absorbance was then measured at 450 nm using a microplate reader.

The effects of Feb-1 on the cell viability of the HT22 cell line and the VSC4.1 cell line were identified using CCK-8. Following the removal of the original medium, a fresh medium containing appropriate concentrations of 0.1 % DMSO solution in PBS or RSL3 (2 μM) or RSL3 (2 μM) + Feb-1 (1 μM) was added. The cells were then incubated at 37 °C for 12 h. Following the addition of CCK-8, the samples were incubated in a 37 °C incubator for 2 h, and then the absorbance was measured using a microplate reader. The plates were placed in a microplate reader (ELx800; Bio-Tek) to detect the absorbance at 450 nm.

2.9. Reactive oxygen species detection

The ROS assay kit (Catalog# S0033S; Beyotime) was employed to assess intracellular ROS levels in Huc-MSCs. Following the removal of the original medium, fresh medium containing appropriate concentrations of 0.1 % DMSO solution in PBS or RSL3 (6 μM) or RSL3 (6 μM) + Fer-1 (1 μM) or RSL3 (6 μM) + Feb-1 (1 μM) was added. The cells were then incubated at 37 °C for 24 h. DCFH-DA was diluted to 1: 1000 with serum-free MEM medium (final concentration 10 μM). After incubation at 37 °C for 20 min, intracellular ROS was detected using a fluorescence microscope (Cat# TH4-200; Olympus) at Ex/Em = 488/525 nm.

2.10. GSH detection

A GSH assay kit (Cat# BC1175; Solarbio) was used to determine the total GSH levels in Huc-MSCs. The control cells were treated with a 0.1 % DMSO solution in PBS. Other cells were treated with RSL3 (6 μM), RSL3 (6 μM) + Fer-1 (1 μM), or RSL3 (6 μM) + Feb-1 (1 μM) for 24 h. After treatment, the cells were digested with trypsin and collected by centrifugation. Subsequently, the concentrations were determined according to the standard manufacturer's instructions. The absorbance was measured at 412 nm, and the GSH content was calculated based on the GSH standard curve.

2.11. Mitochondrial membrane potential (MMP)

JC-1 is a fluorescent probe frequently used for detecting the MMP. Experiments were performed with the JC-1 assay kit (Cat# M8650; Solarbio). Huc-MSCs were treated following exposure to PBS, RSL3 (6 μM), or RSL3 (6 μM) + Tz-A6 peptide (1 μM) + ROS Nano@Feb-1 (Feb-1 concentration of 0.1 nM). After treatment, plates were washed twice with PBS. Subsequently, cells were incubated in a staining solution for 30 min and placed in the 37 °C incubator. After staining, cells were washed twice. The staining buffer was replaced with MEM medium (Cat#C11095500BT; Gibco-Invitrogen) and plates were placed under a fluorescence microscope (Leica, DMi8, GER). Finally, images were acquired using fluorescence microscopy and quantified using Image J (NIH).

2.12. Dihydroethidium staining

The HT22 cell line and the VSC4.1 cell line were inoculated into 24-well plates at 30,000 per well. The plates were then cultured for an additional 24 h. Cells were divided into groups and treated with DMEM complete culture medium, DMEM complete culture medium containing 2 μM RSL3, or DMEM complete culture medium containing 2 μM RSL3 and 1 μM Feb-1, and incubated for 12 h. A solution of dihydroethidium (5 μM) (Cat# S0063; Beyotime) was added to each culture well, and the cells were co-incubated at 37 °C for 30 min for fluorescent probe loading. Afterward, the cells were gently washed once with PBS buffer and observed and photographed under a fluorescence microscope. ImageJ was used for image quantification.

2.13. Pharmacokinetics of Feb-1 in vitro

The Feb-1 was dissolved in DMSO to create a working solution with a concentration of 500 μg/mL. Then, 5.0 μL of the working solution was added to 495.0 μL of fresh rat serum, resulting in a final solution with a concentration of 5 μg/mL. The mixture was then placed in a 37 °C water bath and incubated for 6 h with specific time intervals (0 h, 0.25 h, 0.5 h, 1 h, 3 h, and 6 h). At each time point, a 50 μL mixture was separated and mixed with 150 μL of cold acetonitrile immediately, further lyophilized in tubes, and stored at −80 °C until LC-MS detection. Before performing LC-MS analysis, the samples were diluted in 100 μL acetonitrile containing Salvianolic acid B (0.1 mg/mL) as internal standard (IS). The samples were vortexed and sonicated for 5 min. The mixture was centrifuged at 13,000 rpm for 5 min at 4 °C to remove the precipitation. Then the supernatant was transferred to an HPLC-MS chromatography vial (Thermo Scientific, Vanquish UPLC; Acquity UPLC BEH C18 1.7 μm, 2.1 × 100 mm column). The quantitative analysis of Feb-1 and its metabolic intermediates was then quantified using an extracted-ion chromatogram (EIC) mass spectrometry (Thermo Scientific, Orbitrap Exploris 480).

2.14. Feb-1 drug efficacy post-metabolism in vitro

Feb-1 samples were dissolved in DMSO to prepare a stock solution with a concentration of 10 mM. Before use, the stock solution was

diluted to the desired working concentration of 1 mM. Adequate fresh rat serum was prepared in advance and stored at 2–8 °C. A mixture of 396 μL of rat serum sample and 4 μL of Feb-1 working solution was prepared, resulting in a final concentration of Feb-1 of 10 μM, and pre-incubated at 37 °C. The mixed system was then placed in a 37 °C water bath, and samples were taken at corresponding time points (0 h, 0.25 h, 0.5 h, 1 h, 3 h, and 6 h). At each time point, 100 μL of the sample was quickly mixed with 300 μL of cold acetonitrile, vortexed for 3 min, and centrifuged at 13,000 rpm for 3 min. The supernatant serum extracts were collected and freeze-dried.

The dried serum extracts were re-dissolved in 10 μL of DMSO and subsequently added to 1 mL of medium containing 2 μM RSL3 according to subgroups and set aside. The HT22 cell line was incubated at 8000 per well in 96-well cell culture plates for 12 h. Following the removal of the original medium, fresh medium containing PBS or RSL3 (2 μM) or RSL3 (2 μM) + serum extracts from different subgroups were added. The cells were then incubated at 37 °C for 12 h. Following the addition of CCK-8, the samples were incubated in a 37 °C incubator for 2 h, and then the absorbance was measured using a microplate reader. The plates were placed in a microplate reader (ELx800; Bio-Tek) to detect the absorbance at 450 nm.

2.15. Biodistribution profile of Feb-1 in organs and blood

Wistar rats aged 8 weeks (190 g–210 g) were injected intraperitoneally with Feb-1 (0.8 mg/kg). The biodistribution of prodrug Feb-1 was assessed at 0.5, 1, 3, and 6 h after intraperitoneal injection. Individual organs of rats (heart, liver, spleen, lungs, kidneys, spinal cord) were collected on dry ice at necropsy, and then 100 mg of tissue was taken from each organ and further homogenized. At the same time, 100 μL blood of each rat was collected in heparin tubes. The obtained tissues and blood were homogenized in 400 μL ACN: H_2O (v: v = 3: 1) solution, further lyophilized in tubes, and stored at −80 °C until analysis. Before performing LC-MS detection, these samples were diluted in 100 μL acetonitrile containing salvianolic acid B (0.1 mg/mL) as internal standard (IS). The samples were vortexed and sonicated for 5 min. The extracts were centrifuged at 13,000 rpm for 10 min at 4 °C twice to remove the precipitation. Then the supernatant was transferred to an HPLC-MS chromatography vial. At each time point, the quantitative analysis of Feb-1 and its metabolic intermediates was then quantified using extracted-ion chromatogram (EIC) mass spectrometry with the same UPLC-MS system as described above.

2.16. SCI model

Female Wistar rats aged 8 weeks (190 g–210 g) have been used in this experiment. All the animals from Beijing Vital River Laboratory Animal Technology Co., Ltd. The rats were first acclimatized to the new housing environment for 5 days. All surgeries were performed in a sterile, temperature-appropriate operating theatre. After weighing, rats were anesthetized with isoflurane (RWD life science, China). Anesthesia is maintained with 2–3% isoflurane. The modified Allen's method was used to create a contusion SCI model. All animal experiments have been approved by the Ethics Committee.

An approximately 1 cm incision was made on the back at the T10 thoracic vertebrae. The muscles and fascia around the vertebrae were carefully separated layer by layer to expose the lamina. Subsequently, the lamina of the T10 segment was removed to expose the spinal cord. An NYU Impact Model III (WM Keck, USA) was employed to induce the SCI contusion model. The contusion SCI model was created using the Impact Model III. The weight of the impactor was 10 g, and the height of the free fall was 2.5 cm. Following the impact, the muscles and skin were sutured layer by layer. Bladder evacuation was gently performed twice a day for the first 7 days post-injury until spontaneous urination was restored.

The rat experiments comprised five groups: Sham, SCI, Feb-1, Feb-1 + MSCs, and Feb-1 + MSCs + NPs. The sham group underwent vertebral lamina removal without inducing SCI. The simple injury group received in situ injections of PBS on the seventh day after SCI. The Feb-1 group, Feb-1 + MSCs group, and Feb-1 + MSCs + NPs group were administered intraperitoneal injections of Feb-1 (0.8 mg/kg) immediately after SCI for 7 consecutive days. On the seventh day after injury, the Feb-1 group, Feb-1 + MSCs group, and Feb-1 + MSCs + NPs group were respectively transplanted with PBS, MSCs, or MSCs carrying NPs via Tz-A6 peptide using a microinjector.

2.17. Western blot (WB)

Following cardiac perfusion of the rats with PBS solution, a 1 cm section of spinal cord tissue was extracted from the injury epicenter of each rat. For both cellular and spinal cord samples, we used RIPA lysis buffer (Cat# P0013B; Beyotime) for lysis. The lysate contains protease and phosphatase inhibitor cocktail (Cat# P1045; Beyotime). Lysis was carried out on ice for 30 min, followed by centrifugation using a centrifuge. Protein content was determined using BCA on the supernatant after completion of centrifugation (Cat# P0009; Beyotime). Protein samples are mixed with loading buffer and boiled at 95 °C for 5 min.

According to the results of the BCA assay, protein samples were electrophoresed on 12.5 % SDS-PAGE gel. The total proteins were transferred to the PVDF membrane in transfer buffer (wet) for subsequent operations. We selected GPX-4 (1: 2500; Cat# ab125066; Abcam), xCT (1: 2500; Cat# 26864-1-AP; Proteintech) and Beta Actin (1: 2500; Cat# 81115-1-RR; Proteintech) iNOS (1: 2500; Cat# ab178945; Abcam) IL-1 beta (1: 2500; Cat# ab254360; Abcam) used as primary antibodies with an incubation time of 2 h at RT. Secondary antibodies were HRP-linked anti-rabbit IgG (1:2500; Cat# 7074; CST). An ECL substrate kit (Cat# P0018S; Beyotime) was used to visualize the bands.

2.18. Nissl staining

Rats from different experimental groups were euthanized on the tenth day post spinal cord injury and their spinal cord tissue was removed for Nissl staining. Nissl staining was performed using the Nissl Stain Kit (Methylene Blue Method) (Cat# G1434, Solarbio). Frozen coronal sections of spinal cord tissue (8 μm thick) were taken out and thawed, then immersed in distilled water. The sections were placed in Methylene Blue Stain and incubated at RT for 10 min. After termination of staining, the sections were differentiated in Nissl differentiation solution for 3 min and observed under the microscope. Treat in Ammonium Molybdate Solution for 3 min then rinse with distilled water to avoid decolorisation. Subsequently, the tissues were rapidly dehydrated with absolute ethanol and cleared in xylene before being mounted with neutral gum. Images of the injured site in the rat spinal cord were captured, with Nissl bodies stained blue in the spinal cord tissue while the background appeared colorless. Data were recorded and analyzed accordingly.

2.19. Immunofluorescence staining (IF)

After the rats were initially perfused with PBS solution, a subsequent perfusion was conducted using a 4 % formaldehyde solution. A 2 cm long section of spinal cord tissue from the injury epicenter was continued to be fixed in 4 % formaldehyde at 4 °C for 24 h. The tissue was dehydrated in a sequential manner in 10 %, 20 %, and 30 % sucrose solutions, each for one day. Subsequently, the tissue was embedded in optimal cutting temperature (OCT) compound and stored at −20 °C. Afterward, using a frozen microtome (CM30505 Leica), the spinal cord was cut into 6 μm thick cryosections. All cryosections were washed for 5 min in 1 × PBS to remove OCT. Then, the cryosections were blocked with PBS containing 0.25 % Triton X-100 (Cat# T8200; Solarbio) and 5 % BSA (Cat# A8020; Solarbio) at RT for 1 h.

GFAP (1: 500; Cat# ab279289; Abcam) and NeuN (1: 500; Cat#

ab177487; Abcam) were selected as primary antibodies with an incubation time of 2 h at RT. After circling the appropriate range on the slide with a PAP pen, the primary antibodies were added and incubated for 2 h at RT. Goat Anti-Mouse IgG (Alexa Fluor® 555) (1: 400; Cat# ab150118; Abcam) and Goat Anti-Rabbit IgG (Alexa Fluor® 488) (1: 400; Cat# ab150081; Abcam) were used as secondary antibodies for incubation. After washing, sections were covered and slipped with a mounting medium containing DAPI (Cat# ab104139; Abcam).

2.20. BBB score

The locomotory behavior of rats was assessed by BBB score [36]. Scoring was performed 1day post-injury (dpi) and 3 dpi before SCI. Then, the BBB score was evaluated every 7 dpi. Rats were placed in an open space and moved freely. Scoring was independently conducted by two experimenters. The score included multiple parameters, such as paw movement and joint movement. The scoring ranged from 0 to 21.

2.21. HE staining

After perfusion of the rats with PBS solution, they were further perfused with a 4 % formaldehyde solution. The tissues were then embedded in OCT and frozen at −20 °C. Subsequently, the tissues were cut into 6 μm sections. HE staining was then performed according to the instructions provided in the kit (Cat#C0105S; Beyotime).

2.22. Catwalk gait analysis

A fully automated gait analysis Catwalk XT system (version 10.6, Noldus)was performed 6 weeks after SCI [37]. One week before the Catwalk test, the rats were pre-trained to cross the illuminated walkway. Between the individual rats, the track was carefully wiped down with a 1 % alcohol solution and dried to reduce the possibility of odor interference. The experimental data were analyzed using Catwalk XT system software.

2.23. Motor-evoked potentials

In rats from various treatment groups, motor-evoked potentials (MEPs) were assessed 6 weeks post SCI in anesthetized animals to evaluate nerve conduction function [38]. The stimulation electrode was placed on the representative hindlimb area of the motor cortex, and a series of five consecutive 10 mA stimuli were administered using electrophysiological equipment (YRKJ-G2008; Zhuhai Yiruikeji Co., Ltd). The recording electrode was placed in the lower limb calf gastrocnemius [39]. Amplitude and latency were quantified using Image J Software.

2.24. Statistical analysis

Data were expressed as mean value ± SEM for at least three independent biological replicates. The plots were generated, and all the statistical analyses were carried out using GraphPad Prism 9.0. (GraphPad Software, Inc., San Diego, CA, USA). Statistics were considered significant at a P value of 0.05.

3. Results

3.1. Preparation and characterization of ROS-responsive nanoparticles

Considering the different click chemical handles will have different reaction rates when designing amphiphilic carriers, we borrowed from some published nanocarriers and selected the TCO group as a hydrophobic click chemical center to ensure the efficiency of the conjugation reaction [40–42].

For the preparation of ROS-responsive nanoparticles conjugated with Huc-MSCs, the polymer mPEG-b-Lys-BECI-TCO was synthesized, consisting of a mPEG-based hydrophilic segment and a hydrophobic fragment with ROS scavengers and bio-orthogonal handles (Fig. 1). Of note, the block copolymer exhibits amphiphilic properties, where the benzeneboronic acid pinacol ester would be cleaved gradually under the action of ROS and release the more hydrophilic lysine side chain (Fig. 2a). The structure of mPEG-b-Lys-BECI-TCO polymer was confirmed by ^{1}H NMR spectrum (Fig. S4). In this study when mPEG-b-Lys-BECI-TCO was used as a drug or dye carrier to form nanoparticles, we called the nanoparticles ROS Nano. When a nanoparticle carries a certain drug, such as Feb-1, we name this nanoparticle ROS Nano@Feb-1.

We used flash nanoprecipitation method [43] to synthesize the polymeric nanocarriers. Both transmission electron microscopy and scanning electron microscopy images showed that nanoparticles exhibit a spherical morphology (Fig. 2b–h). The diameters of the nanodrugs were about 105 nm without the hydration layer (Fig. 2b). And the size was approximately 107 nm measured by nanoparticle tracking analysis (NTA) (Fig. 2c) and dynamic light scattering (DLS) (Fig. 2d). The surface potentials of the ROS Nano@Feb-1 was nearly −23 mV, revealing neutralization (Fig. 2e). The obtained ROS-responsive nanocarriers encapsulated the prodrug Feb-1 within its core, achieving moderate encapsulation efficiency (EE = 51.12 %) and loading capacity (LC = 20.36 %).

Different concentrations of H_2O_2 solutions were used to simulate high ROS microenvironments. To evaluate the ROS responsiveness of ROS Nano@Feb-1, the micelle was incubated in H_2O_2 solutions for 1 h. The results showed that ROS Nano@Feb-1 was able to accelerate the release of Feb-1 in the presence of ROS (Fig. 2f and g). The morphological changes of the nanoparticles were characterized by transmission electron microscopy. We found that the diameters of the nanodrugs enlarged due to the H_2O_2 stimulation, and confirmed observable expansion and disintegration (Fig. 2h and i), which is consistent with the earlier findings. The H_2O_2 stimulation increased the hydrophilicity of the nano polymer and decreased the zeta potential (Fig. 2j), which may be the reason for the increase in nanoparticle diameter [34,44,45]. Together, ROS Nano@Feb-1 is moderately stable and capable of accelerating the release of Feb-1 in the presence of ROS.

Although the A6 peptide (sequence: Ac-KPSSPPEE-NH2) has been clinically proven to deliver drugs to metastatic tumors by specifically binding to the CD44 membrane protein [46,47], there are rare reports on drug delivery systems by binding to CD44 of transplanted Huc-MSCs. To validate the design, we analyzed the immunophenotype of Huc-MSCs by flow cytometry and confirmed the high positive expression of CD44 in Huc-MSCs (Fig. S5). Subsequently, a maleimide-modified tetrazine (Mal tetrazine) was synthesized and subsequently incubated with A6 peptide. Then, the functionalization of A6 peptides with tetrazine as bio-orthogonal handles (Tz-A6 peptide) was successfully established and confirmed using NMR, HRMS, and HPLC analysis (Figs. S6–10).

To verify that the Tz-A6 peptide-based cell-loaded nanoparticle delivery system could be docked, we used DID as a probe for the tracer. Huc-MSCs were first incubated for 5 min with medium containing 1 μM Tz-A6 peptide versus medium without Tz-A6 peptide. Subsequently, after a short co-incubation with ROS Nano@DID, imaging was performed using fluorescence microscopy (Fig. 2k-l). The results confirmed that Tz-A6 peptide could promote the docking of nanoparticles to Huc-MSCs. In conclusion, these results suggested that ROS-responsive micelles have been successfully constructed and enable cell-loaded nanoparticles via the Tz-A6 peptide.

3.2. Synthesis and characterization of Feborastatin-1 (Feb-1)

Although Ferrostatin-1 (Fer-1) has been a commonly used compound in ferroptosis research, findings suggest that its application is limited in vivo because of poor metabolic stability [48]. Researchers have continuously tried to give Fer-1 better metabolic stability by introducing protective chemical groups into it [42]. In this article, we report the

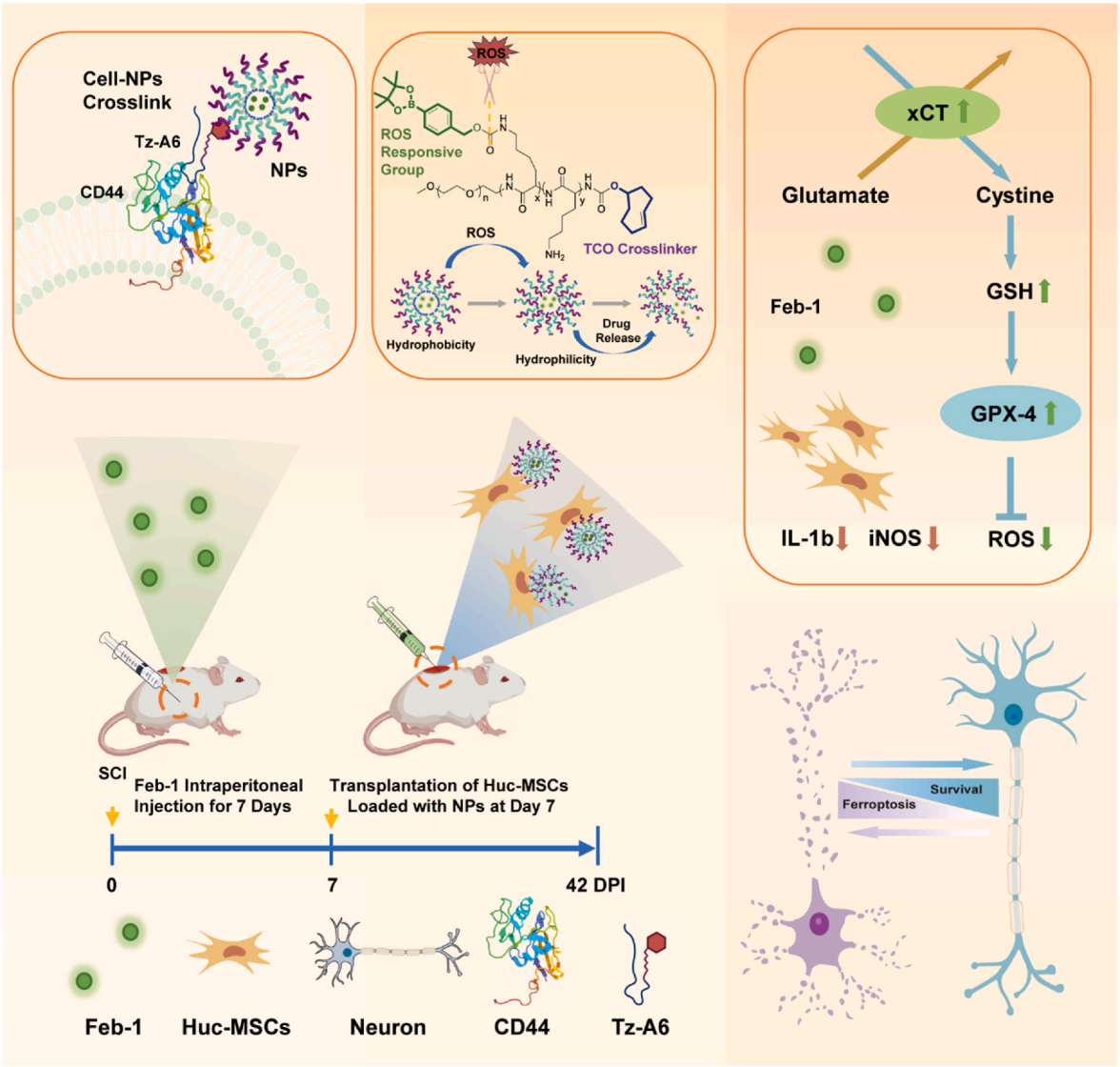

Fig. 1. Construction of ROS-responsive nanoparticles and the mechanism of repairing spinal cord injury. (a) ROS Nano@Feb-1 was prepared using mPEG-b-Lys-BECI-TCO as a nanocarrier. Tz-A6 peptide binds to CD44 on the surface of Huc-MSCs and then connects with ROS Nano@Feb-1 via click chemistry thereby enabling cellular drug–carrying. The ROS-induced reaction prompts the cleavage of the mPEG-b-Lys-BECI-TCO hydrophobic boronic acid ester, leading to the formation of hydrophilic residues followed by the release of the drug. At first, Feb-1 was administered intraperitoneal injections immediately after SCI for 7 consecutive days. Then the Huc-MSCs which carry NPs via Tz-A6 peptide were injected into the center of the injury using a microinjector on the seventh day after SCI. The Feb-1 reduced ferroptosis after SCI by promoting xCT and GPX4 expression. The treatment combination of Feb-1, Huc-MSCs, and NPs produces beneficial therapeutic effects, promoting SCI repair.

synthesis of a viable Fer-1 analog (Fig. S11a) that potently inhibits ferroptosis and is named Feborastatin-1 (Feb-1). Complex Feb-1 was synthesized by conjugated Fer-1 with a phenylboronic ester as a temporary masking group [49], followed by chromatography for purification. The final product was fully characterized by high-resolution mass spectrometry (HRMS), ^{1}H NMR, and ^{13}C NMR (Figs. S11 and 12).

Further analysis of the stability of Feb-1 indicated that its drug half-life ($T_{1/2}$) in rat serum is 0.25 h, slightly better than Fer-1 (Fig. S13). The preliminary biodistribution and pharmacokinetics of Feb-1 were investigated to confirm the stability and efficiency of in vivo conditions. Significant concentrations of Feb-1 and its active pharmaceutical ingredients (AIP) were found in all analyzed tissues (Figs. S14–17). The distribution analysis indicated that the Feb-1 and its APIs were retained via intraperitoneal injection.

3.3. Validation of Feborastatin-1 (Feb-1) drug efficacy

To verify the cytotoxicity of Fer-1 and Feb-1 at different concentrations we examined Huc-MSCs viability using CCK-8. The results confirmed that both drugs had no significant effect on cell viability at concentrations below 1 μM (Fig. 3a). However, we found that Feb-1 was more cytotoxic than Fer-1 at a drug concentration of 10 μM. From this, we conjecture that the structure of phenylboronic ester may enhance the antioxidant capacity of the drug, thus leading to the disruption of cellular oxidative homeostasis. It has been reported that Fer-1 can directly resist H_2O_2-induced cell death [50]. Subsequently, we detected H_2O_2-induced Huc-MSCs death using CCK-8. The results indicated that drug concentrations in the range of 100–1000 nM were both successful in rescuing H_2O_2-induced cell death (Fig. 3c–e). Yet, Fer-1 and Feb-1 did not express a statistically significant difference at different concentrations.

We then further validated the resistance of Fer-1 and Feb-1 to

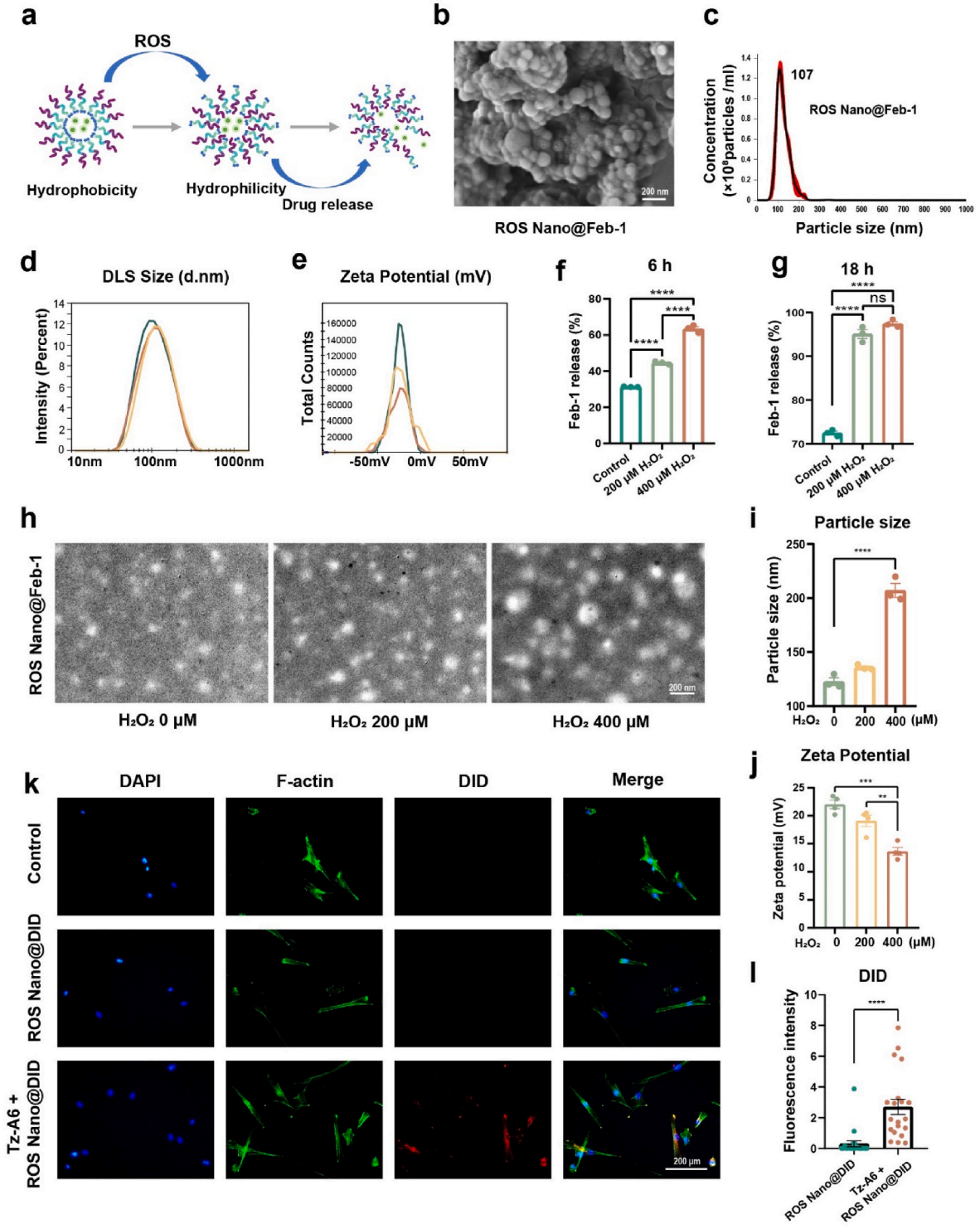

Fig. 2. Characterization of ROS Nano@Feb-1. (a) Mechanism of drug release from ROS Nano@Feb-1. ROS Nano@Feb-1 consumes ROS and releases Feb-1 by responding to excess ROS after injury. (b) ROS Nano@Feb-1 morphology under scanning electron microscopy. ROS Nano@Feb-1 is a uniform spherical particle with a size of about 105 nm, scale bar = 200 nm. (c) NTA analysis of ROS Nano@Feb-1 particle size distribution. NTA analysis indicates that ROS Nano@Feb-1 particle size is concentrated at 107 nm. (d–e) DLS and Zeta Potential analysis of ROS Nano@Feb-1 (n = 3). (f–g) Drug release rates of ROS Nano@Feb-1 in different solutions (n = 3, one-way ANOVA, Tukey's post hoc tests, $^{****}P < 0.0001$). (h–i) Transmission electron microscopy images analysis of ROS nano after 1 h of H_2O_2 oxidation (n = 3, one-way ANOVA, Tukey's post hoc tests, $^{****}P < 0.0001$). The particle size increased after the H_2O_2 oxidation treatment, scale bar = 200 nm. (j) Zeta potential analysis of ROS Nano@Feb-1 after incubation with different concentrations of H_2O_2 solution for 1 h (n = 4, one-way ANOVA, Tukey's post hoc tests, $^{**}P < 0.01$, and $^{***}P < 0.001$). (k–l) Tz-A6 peptide could promote the docking of ROS Nano@DID nanoparticles to Huc-MSCs, scale bar = 200 μm. (n = 20, one-way ANOVA, Tukey's post hoc tests, $^{****}P < 0.0001$).

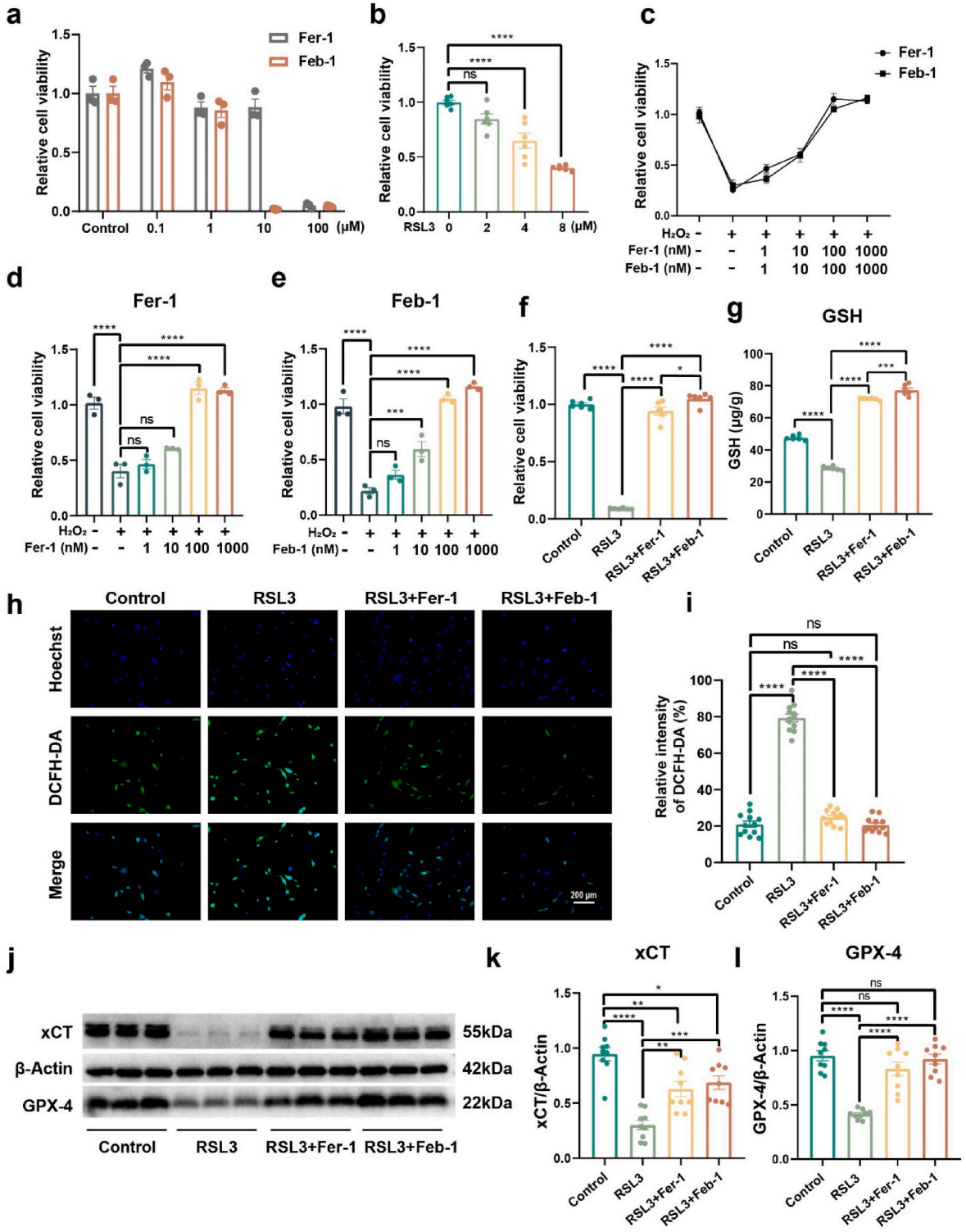

Fig. 3. In vitro validation of Feb-1 drug effectiveness. (a) The effects of Feb-1 and Fer-1 on cell viability of Huc-MSCs were identified using CCK-8 (n = 3, one-way ANOVA, Tukey's post hoc tests). The results indicate that the drug has no obvious effect on cell viability at drug concentrations below 1 μM. (b) Exploring the appropriate concentration of RSL3 to induce ferroptosis (n = 6, one-way ANOVA, Tukey's post hoc tests, ****$P < 0.0001$). (c–e) Rescue of H_2O_2-induced cell death in Huc-MSCs by different concentrations of Fer-1 and Feb-1. (n = 6, one-way ANOVA, Tukey's post hoc tests, ***$P < 0.001$, and ****$P < 0.0001$). (f) Rescue of RSL3-induced ferroptosis by Feb-1 and Fer-1 at 1 μM concentration. Ferroptosis induction was performed using a 6 μM concentration of RSL3 (n = 6, one-way ANOVA, Tukey's post hoc tests, *$P < 0.05$, and ****$P < 0.0001$). (g) Quantitative detection of intracellular GSH (n = 6, one-way ANOVA, Tukey's post hoc tests, ****$P <$ 0.0001). (h–i) Quantification of intracellular ROS using DCFH-DA (green), scale bar = 200 μm (n = 12, one-way ANOVA, Tukey's post hoc tests, ****$P < 0.0001$). (j–l) Western blot analyzed the effect of Feb-1 and Fer-1 on RSL3-induced ferroptosis. Feb-1 rescued the RSL3-induced decrease in GPX-4 and xCT protein expression (n = 9, one-way ANOVA, Tukey's post hoc tests, *$P < 0.05$, **$P < 0.01$, ***$P < 0.001$, and ****$P < 0.0001$).

ferroptosis. As previously reported, RSL3 was used as ferroptosis inducer [51]. Results confirmed that 6 μM RSL3 can suitably induce ferroptosis in vitro (Fig. 3b). Subsequently, the study used CCK-8 to explore the cellular rescue effects of Fer-1 and Feb-1 at a concentration of 1 μM, Feb-1 was slightly more effective than Fer-1 in rescuing cell viability (Fig. 3f). As a major intracellular antioxidant, reduced glutathione (GSH) scavenges peroxides and prevents ferroptosis [52]. Therefore, the experiments further investigated the intracellular level of GSH. The results showed that Feb-1 also more effectively rescued GSH levels (Fig. 3g).

DCFH-DA is cleaved by esterases in the cell and subsequently oxidized by ROS to DCFH, which produces green fluorescence, indicating abnormally high levels of ROS. DCFH-DA analysis revealed that intracellular ROS were markedly increased in the RSL3-induced group,

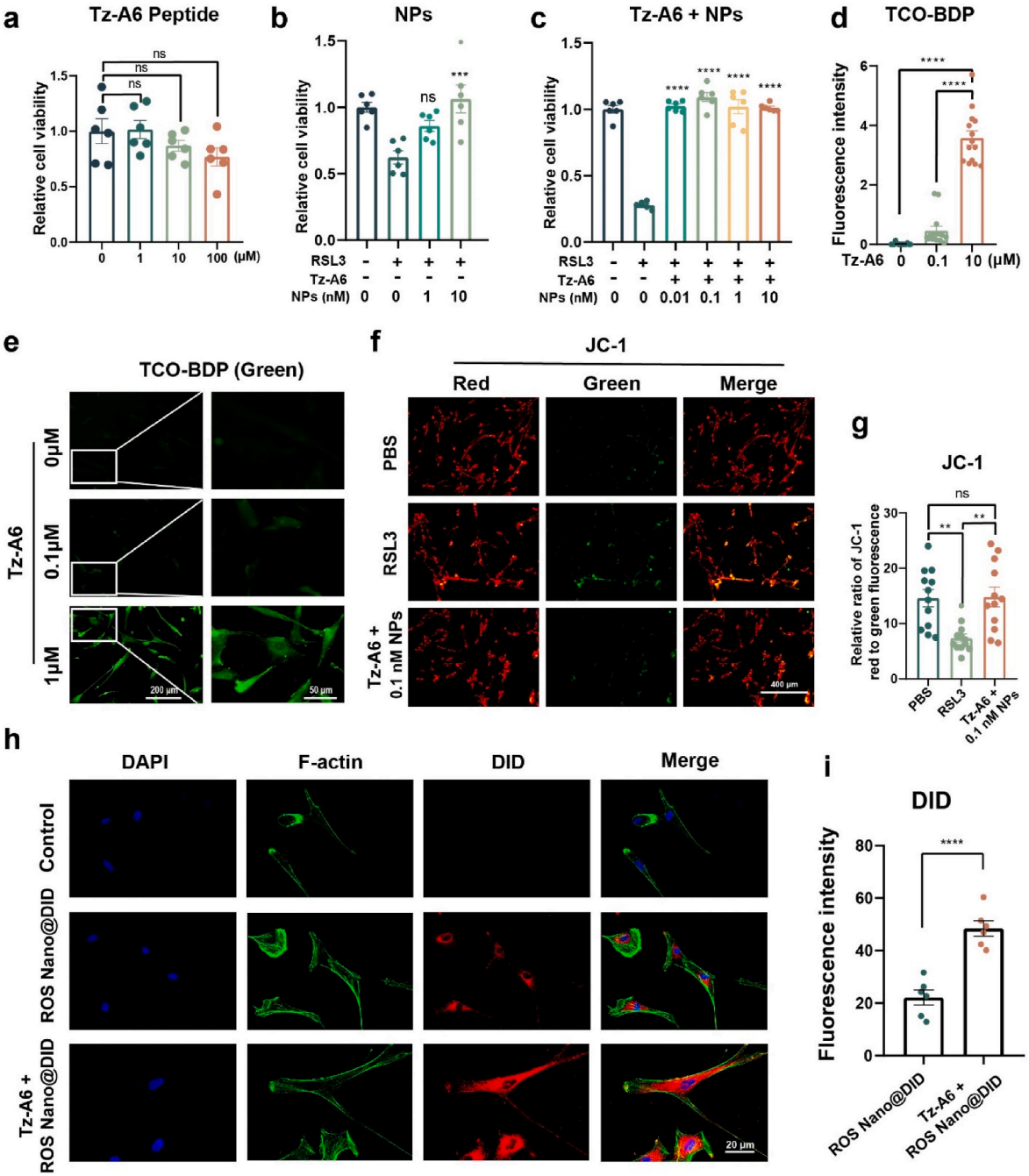

Fig. 4. The ROS-responsive nanoparticles bind to Huc-MSCs by the Tz-A6 peptide. (a) Tz-A6 peptide was tested for its effect on cell viability in Huc-MSCs (n = 6, one-way ANOVA, Tukey's post hoc tests). (b) Rescue of RSL3-induced ferroptosis in Huc-MSCs by ROS Nano@Feb-1 rescue (n = 6 one-way ANOVA, Tukey's post hoc tests, $^{***}P < 0.001$). (c) Rescue of RSL3-induced ferroptosis in Huc-MSCs by ROS Nano@Feb-1 and Tz-A6 peptide (n = 6, one-way ANOVA, Tukey's post hoc tests, $^{****}P < 0.0001$). (d–e) Different concentrations of Tz-A6 peptide were incubated and then added to 1 μM TCO-BDP for staining. Cellular fluorescence increased with increasing concentrations of Tz-A6 peptide; low magnification: scale bar = 200 μm; high magnification: scale bar = 50 μm (n = 14, one-way ANOVA, Tukey's post hoc tests, $^{****}P < 0.0001$). (f–g) After incubation of cells with Tz-A6 peptide at a concentration of 1 μM, ROS Nano@Feb-1 was added at a Feb-1 concentration of 0.1 nM. The results showed that lower concentrations of ROS Nano@Feb-1 in the presence of Tz-A6 peptide rescued RSL3-induced decreases in mitochondrial membrane potential; scale bar = 400 μm. (n = 12, one-way ANOVA, Tukey's post hoc tests, $^{**}P < 0.01$). (h–i) ROS Nano@DID (red) was used to label nanoparticles and phalloidin-YF488 (green) was used to label the cytoskeleton; scale bar = 20 μm. (n = 6, one-way ANOVA, Tukey's post hoc tests, $^{****}P < 0.0001$).

while Feb-1 and Fer-1 could return them to normal levels. (Fig. 3h and i). The study then characterized the indicators related to ferroptosis. GPX-4 and xCT pathways play a functional role in reducing ferroptosis [53]. We detected the expression of xCT and GPX-4 proteins by Western blot assay. Treatment of Huc-MSCs with RSL3 decreased GPX-4 and xCT expression, whereas pretreatment with both drugs markedly restored GPX-4 and xCT expression (Fig. 3j-l).

The experiment further quantified the ability of Feb-1 to rescue cells using Calcein AM/PI staining. Flow cytometry results showed that co-treatment with Fer-1 or Feb-1 prevented RSL3-induced cell death (Fig. S18). In conclusion, these results indicate that the new synthesized compound Feb-1 has the same excellent potency as Fer-1. Moreover, Feb-1 possesses a more stable metabolic structure and shows slightly superior performance than Fer-1 in certain outcomes.

3.4. Capacity of drug loading systems

We first conducted a CCK-8 assay to assess the cytotoxicity of the Tz-A6 peptide to Huc-MSCs. Results confirmed that Huc-MSCs viability was not impacted by the Tz-A6 peptide (Fig. 4a). With the CD44 specific functionalized peptide in hand, the targeting efficacy was first performed using fluorescent labeling in vitro. BDP is a common fluorescent dye, and the study examined Tz-A6 peptide function using TCO-BDP probe, a BDP dye linked with TCO, instead of mPEG-b-Lys-BECI-TCO nanoparticles.

Different concentrations of Tz-A6 peptide were first added to co-incubate with the cells, and TCO-BDP was added after PBS washing. After washing the TCO-BDP, micrographs and fluorescence images were taken. The results indicated a simultaneous increase in fluorescence intensity with increasing Tz-A6 peptide concentration (Fig. 4d and e; Fig. S19). This suggests that the Tz-A6 peptide is able to link TCO-BDP to Huc-MSCs via the Tetrazine-TCO click reaction.

We then used CCK-8 to examine the ability of the ROS Nano@Feb-1 and ROS Nano@Feb-1 + Tz-A6 groups to resist RSL3-induced ferroptosis in cells. The results of the experiment at the concentration of 10 nM suggested that both groups had sound resistance to ferroptosis (Fig. 4b and c). However, we also observed that the group containing the Tz-A6 peptide was able to act at much lower drug concentrations, which was exciting (Fig. 4c).

Therefore, the study examined the reduction of mitochondrial membrane potential using JC-1. The results showed that Feb-1 at a concentration of 0.1 nM did counteract the decrease in mitochondrial membrane potential caused by RSL3 when the Tz-A6 peptide was included (Fig. 4f and g). We speculate that this may be because the presence of Tz-A6 peptide increased the adhesion of ROS Nano@Feb-1 in MSCs [54].

Subsequently, the effect of Tz-A6 peptide on nanoparticle-carried drugs was examined by using ROS Nano@DID. Cells were incubated with medium containing 1 μM Tz-A6 peptide and medium without Tz-A6 peptide for 5 min. After washing out the Tz-A6 peptide, ROS Nano@DID was added and incubated for 15 min. The ROS Nano@DID was washed off after the incubation. Cells were observed using confocal microscopy after incubating in the medium for 2 h. The results showed red fluorescence in all the groups treated with ROS Nano@DID. The use of Tz-A6 peptide led to a marked increase in red fluorescence (Fig. 4h and i). We conjecture that the effect of Tz-A6 peptide in reducing the minimum effective concentration of the drug may be related to its capacity to increase the local drug concentration and to promote drug entry into the cells.

3.5. The treatment promotes neuronal repair by reducing the inflammatory response and ferroptosis

We first wondered whether Feb-1 can reduce ROS and inhibit ferroptosis in nerve cells. The HT22 cell line (mouse hippocampal neuronal cell line) and the VSC4.1 cell line (ventral spinal cord 4.1 motoneurons cell line) were used for experimental validation. Experiments were performed using a 2 μM concentration of RSL3 and a 1 μM concentration of Feb-1. The results showed that Feb-1 was able to antagonize the RSL3-induced reduction in the vitality of both of these cell lines (Fig. 5a and b). The study then characterized the expression of GPX-4 proteins by Western blot assay. Treatment of the VSC4.1 cell line with RSL3 decreased GPX-4 expression, whereas Feb-1 markedly restored (Fig. 5c and d). Superoxide anion is a type of ROS and excess superoxide anion can lead to cellular abnormalities and even death. Dihydroethidium (DHE) staining was used to detect intracellular superoxide anions (Fig. 5e). DHE staining revealed that intracellular superoxide anions were markedly increased in the RSL3-induced group, while Feb-1 could reduce it (Fig. 5f and g).

After verifying that Feb-1 can effectively act as an antioxidant and inhibit ferroptosis in vitro and that the cell-loaded drug delivery system can operate successfully, we attempted to further investigate whether Feb-1 and the delivery system can modulate the post-SCI microenvironment in vivo [55]. We first verified whether Feb-1 could effectively reduce ferroptosis after SCI. We made T10 contusive SCI mode as described previously. Then, three consecutive days of intraperitoneal administration were carried out. The dose for each injection was 0.8 mg/kg. Rats were sacrificed, and spinal cord tissue was removed on the third day. Quantification of GPX-4 as well as xCT protein expression by using Western blot analysis (Fig. 5h). The results revealed that the expression of GPX-4 and xCT showed a notable decrease after SCI and recovered with Feb-1 treatment (Fig. 5i and j).

Experimental evidence suggested that Huc-MSCs promoted SCI repair by reducing the inflammatory response after SCI [56,57]. Further, we tested the role of the cell-loaded drug delivery system on the modulation of inflammatory factors after SCI. To verify the modulation, rats were euthanized on the tenth dpi (i.e., on the third day after cell transplantation), and spinal cord tissues were removed for protein extraction. The Western blot analysis showed that the treatment regimen of Feb-1 + MSCs + NPs significantly reduced the protein expression of iNOS and IL-1b (Fig. 5k, m, n).

To validate the neuroprotective effects of different treatment regimens, we performed Nissl staining on the tenth day after spinal cord injury in rats and statistically analyzed the results (Fig. 5l). The number of neurons remaining 3000–4000 μm from the injury center was counted. The results suggest that the number of neurons decreased significantly after SCI. The number of neurons in the Feb-1, Feb-1 + MSCs, and Feb-1 + MSCs + NPs treatment regimen groups was significantly higher than that in the SCI group (Fig. 5o). The Feb-1 + MSCs + NPs treatment regimen group showed the most neurons and the least damage. Together, the above results suggested that Feb-1 + MSCs and Feb-1 + MSCs + NPs treatment regimen decreased nerve cell death and promoted neuronal recovery, whereas loaded NPs enhanced the effects of the Feb-1 + MSCs treatment regimen.

3.6. The treatment system promotes functional recovery after SCI

To verify the effects of different treatment regimens on the recovery of motor function, we conducted a 6-week behavioral study on rats. The rat experiments consisted of five groups Sham, SCI, Feb-1, Feb-1 + MSCs, Feb-1 + MSCs + NPs. The sham group underwent vertebral lamina removal without inducing SCI. The Feb-1 group, Feb-1 + MSCs group, and Feb-1 + MSCs + NPs group were administered intraperitoneal injections of Feb-1 (0.8 mg/kg) immediately after SCI for 7 consecutive days.

On the seventh day after the injury, the Feb-1 group, Feb-1 + MSCs group, and Feb-1 + MSCs + NPs group were respectively transplanted with PBS, MSCs, or MSCs carrying NPs via Tz-A6 peptide using a microinjector. The SCI group received injections of PBS (Fig. 6a). The number of Huc-MSCs transplanted in Feb-1 + MSCs group, and Feb-1 + MSCs + NPs group was 1×10^6 per rat. The Huc-MSCs of Feb-1 + MSCs + NPs group were first incubated with a medium containing 1 μM Tz-A6

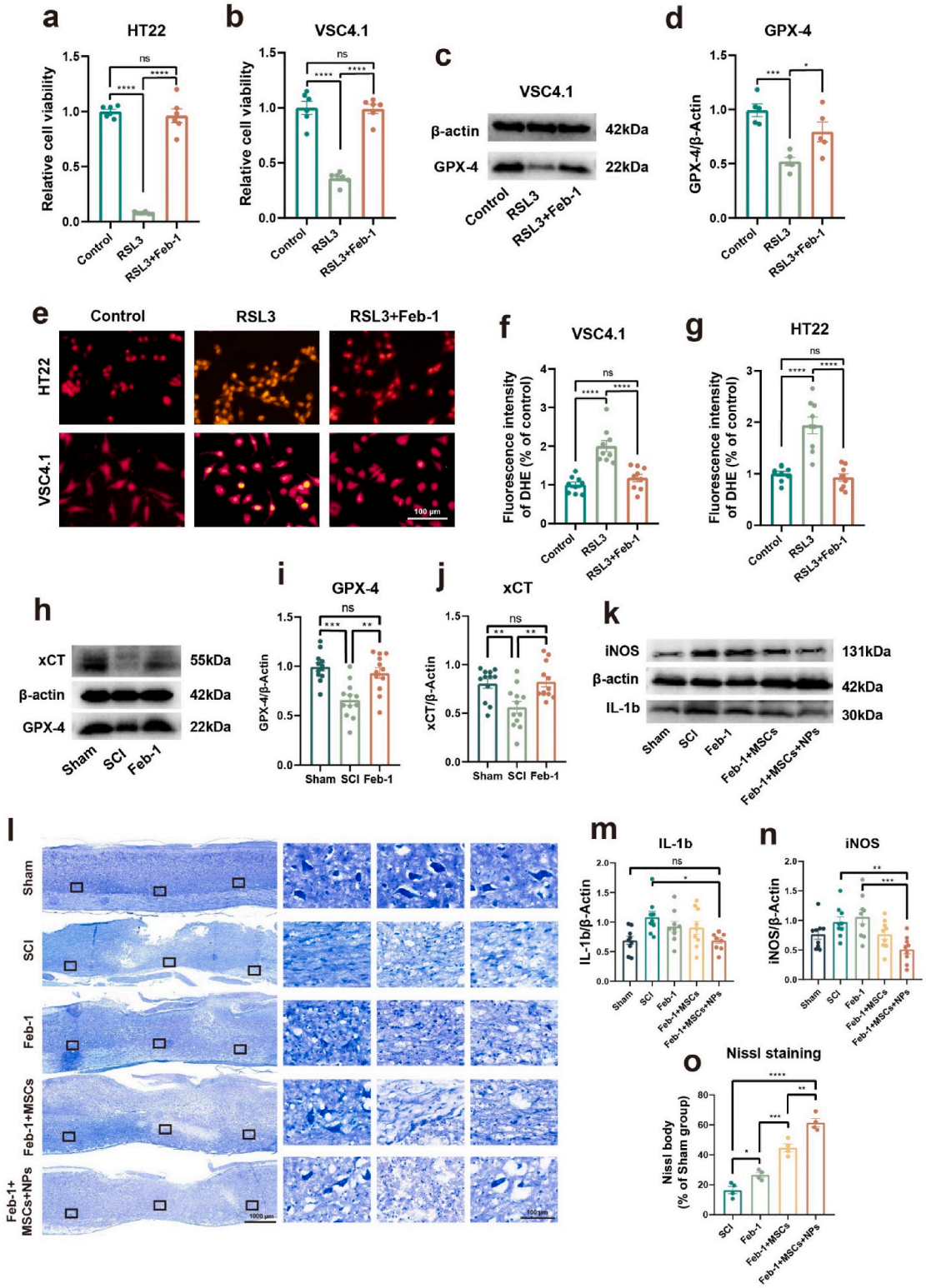

Fig. 5. Feb-1+MSCs+NPs treatment system reduces neuronal cell ferroptosis and modulates inflammation after spinal cord injury (a–b) Feb-1 inhibits ferroptosis in the HT22 cell line and VSC4.1 cell line (n = 6, one-way ANOVA, Tukey's post hoc tests, $^{****}P < 0.0001$). (c–d) Protein expression of GPX-4 in VSC4.1 cell line (n = 5, one-way ANOVA, Tukey's post hoc tests, $^{*}P < 0.05$, and $^{***}P < 0.001$). (e–g) Dihydroethidium staining demonstrated that Feb-1 clears ROS in neuronal cell lines (n = 9, one-way ANOVA, Tukey's post hoc tests, $^{****}P < 0.0001$). (h–j) Protein expression of GPX-4 and xCT in Sham, SCI, and Feb-1 treatment groups 3 dpi (n = 9, one-way ANOVA, Tukey's post hoc tests, $^{**}P < 0.01$, and $^{***}P < 0.001$). (k, m-n) Protein expression of iNOS and IL-1b in the Sham, SCI, and Feb-1 treatment groups 10 dpi (n = 9, one-way ANOVA, Tukey's post hoc tests, $^{*}P < 0.05$, $^{**}P < 0.01$, and $^{***}P < 0.001$). (l, o) The results of Nissl staining showed that different treatment regimens decreased nerve cell death and promoted neuronal recovery (n = 4, one-way ANOVA, Tukey's post hoc tests, $^{*}P < 0.05$, $^{**}P < 0.01$, $^{***}P < 0.001$, and $^{****}P < 0.0001$).

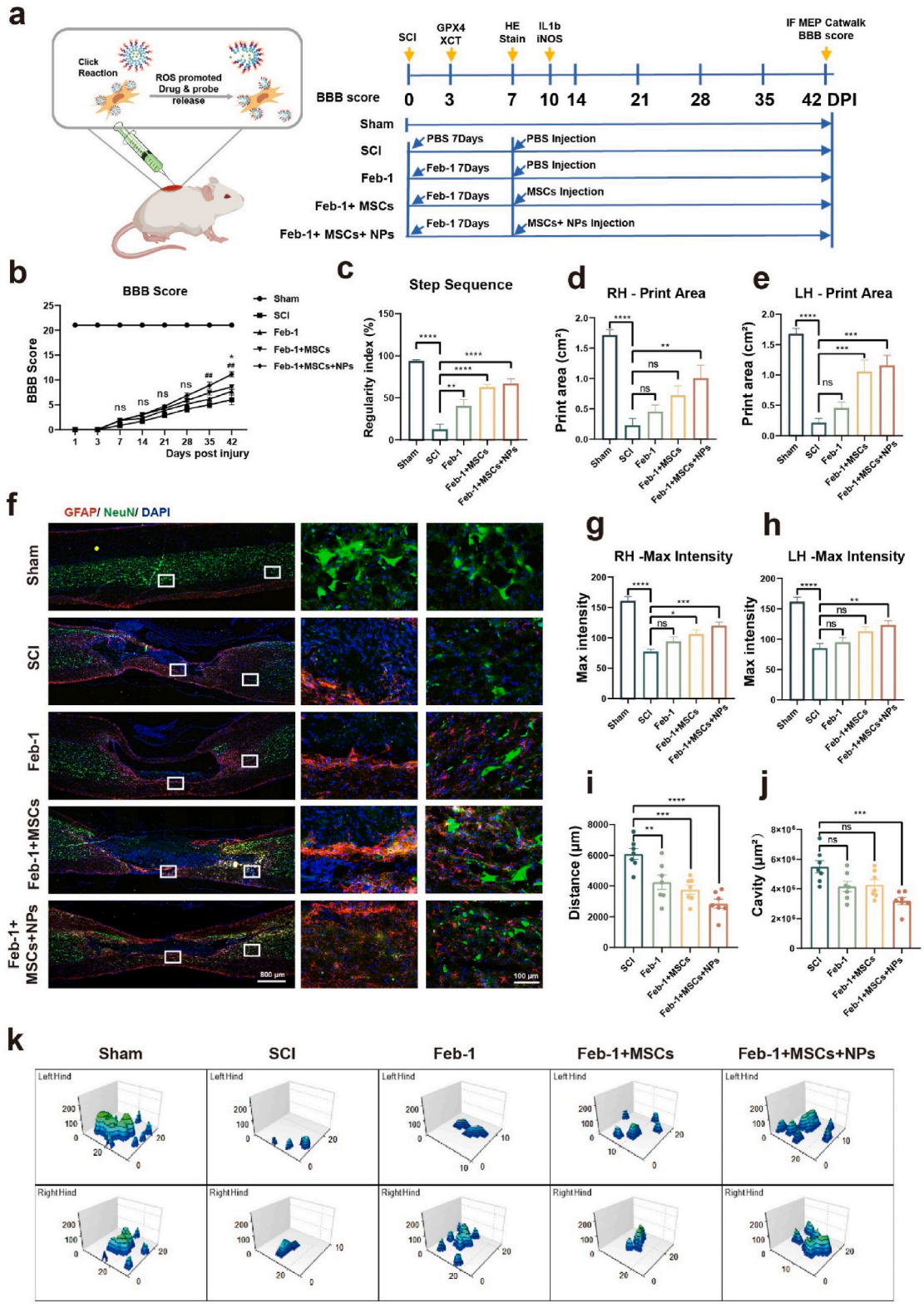

Fig. 6. Systematic evaluation of Feb-1+MSCs+NPs treatment system. (a)Timeline of treatment regimens for rats with spinal cord contusions in the Sham, SCI, Feb-1, Feb-1 + MSCs, Feb-1 + MSCs + NPs groups. (b) BBB scores at 6 consecutive weeks after SCI (n = 7, one-way ANOVA, Tukey's post hoc tests, $^{*}P < 0.05$, $^{\#\#}P < 0.01$, * means the comparison of the Feb-1 + MSCs + NPs and Feb-1 + MSCs group, $^{\#}$ means the comparison of the Feb-1 + MSCs + NPs and Feb-1 group). (c) Catwalk step sequence scores at week six after SCI (n = 7, one-way ANOVA, Tukey's post hoc tests, $^{**}P < 0.01$, and $^{****}P < 0.0001$). (d–e) The mean print area of the rat when passing through the trail (n = 7, one-way ANOVA, Tukey's post hoc tests, $^{**}P < 0.01$, $^{***}P < 0.001$, and $^{****}P < 0.0001$). (f, i-j) Immunofluorescence staining at week six after SCI. GFAP (red) and NeuN (green); scale bar = 800 μm, high magnification: scale bar = 100 μm. (n = 7, one-way ANOVA, Tukey's post hoc tests, $^{**}P < 0.01$, $^{***}P < 0.001$, and $^{****}P < 0.0001$). (g–h) Maximum paw pressure on the ceiling as the rat passes through it (n = 7, one-way ANOVA, Tukey's post hoc tests, $^{*}P < 0.05$, $^{**}P < 0.01$, $^{***}P < 0.001$, and $^{****}P < 0.0001$). (k) 3D reconstruction of the pressure on rat paws contacting the ceiling.

peptide for 5 min, followed by 15 min in incubation with 1 μM ROS Nano@Feb-1. The ROS Nano@Feb-1 loading on the Huc-MSCs in the Feb-1 + MSCs + NPs group was detected by HPLC-MS to be nearly 25 μg of Feb-1 and its APIs were loaded per 1 million cells (Fig. S20).

Initially, we evaluated the in vivo toxicity of Feb-1. We constructed a rat spinal cord contusion model and injected Feb-1 intraperitoneally for 7 consecutive days after injury. The dose for each injection was 0.8 mg/kg and the spinal cord tissue was extracted on day seven [58]. The hearts, livers, spleens, lungs, and kidneys of rats were cryosectioned and identified by HE staining to evaluate drug effects. The results confirmed that the drug did not cause organ toxicity (Fig. S21). No organ toxicity was observed in the Feb-1 + MSCs + NPs treatment regimen via HE staining and plasma biochemical parameters level detection, including AST, ALT, UA, CREA, and UREA (Fig. S22).

Motor function recovery in different treatment regimens was evidenced by BBB scores Catwalk analysis and motor-evoked potentials

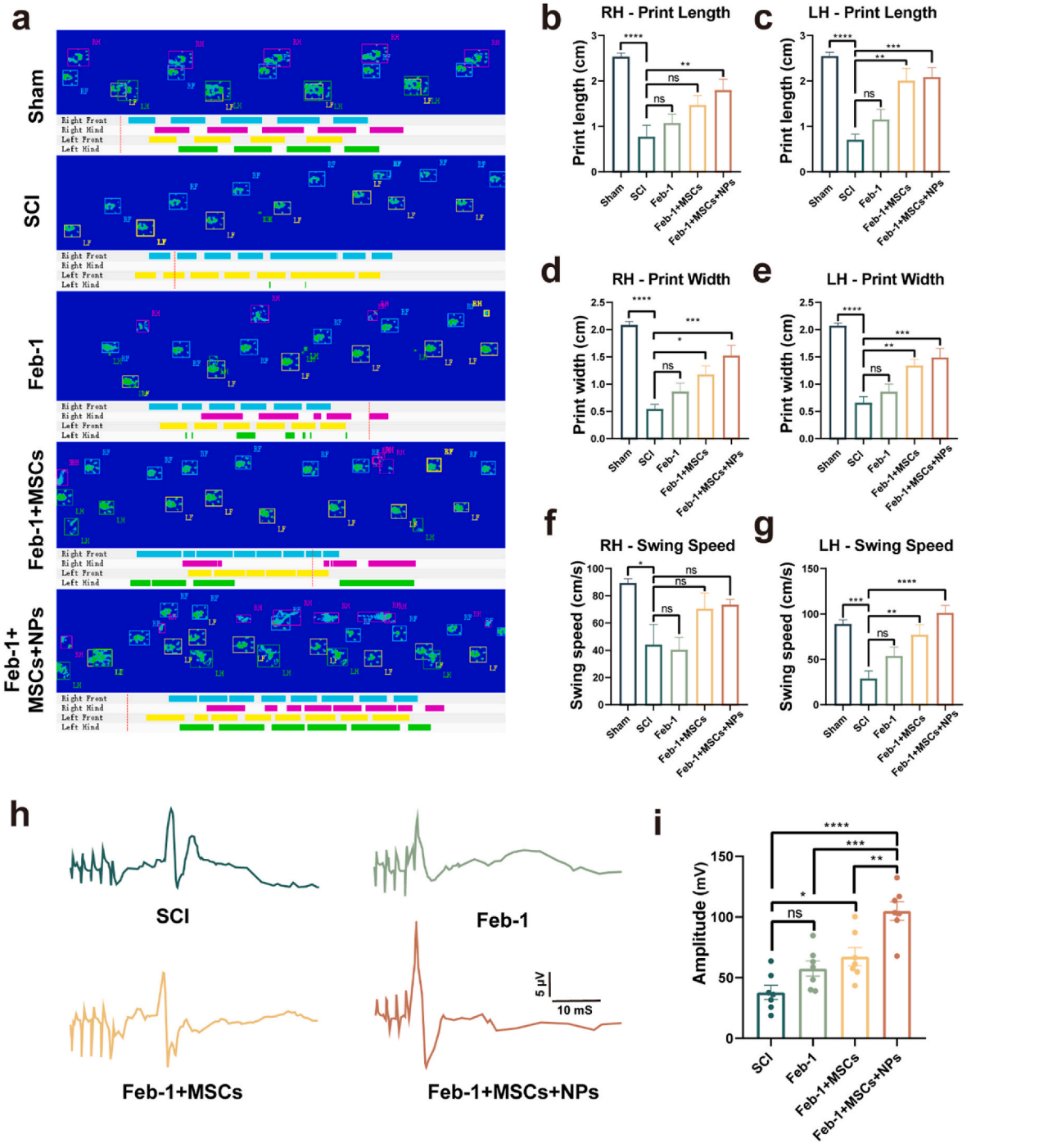

Fig. 7. Feb-1+MSCs+NPs treatment promotes functional recovery in SCI rats. (a) Typical diagrams of Catwalk test in Sham, SCI, Feb-1, Feb-1 + MSCs, Feb-1 + MSCs + NPs group of rats at week 6 post-injury. (b–c) Print length of the left and right hind limbs (n = 7, one-way ANOVA, Tukey's post hoc tests, $^{**}P < 0.01$, $^{***}P < 0.001$ and $^{****}P < 0.0001$). (d–e) Print width of the left and right hind limbs (n = 7, one-way ANOVA, Tukey's post hoc tests, $^{*}P < 0.05$, $^{**}P < 0.01$, $^{***}P < 0.001$ and $^{****}P < 0.0001$). (f–g) Swing speed for hind-limb after treatment (n = 7, one-way ANOVA, Tukey's post hoc tests, $^{*}P < 0.05$, $^{**}P < 0.01$, $^{***}P < 0.001$, and $^{****}P < 0.0001$). (h–i) MEP analysis for electrophysiological evaluation at week 6 post-injury. Quantification of MEP peak-to-peak amplitude in rats of different treatment groups (n = 7, one-way ANOVA, Tukey's post hoc tests, $^{*}P < 0.05$, $^{**}P < 0.01$, $^{***}P < 0.001$, and $^{****}P < 0.0001$).

(MEPs). The treatment regimen with Feb-1 alone had higher Catwalk step sequence analysis scores than the SCI group (Figs. 6c and 7a). This suggests that the Feb-1-alone regimen has some, but limited, efficacy in functional recovery in SCI. The Feb-1 + MSCs regimen started with significantly higher BBB scores than the SCI group at week 5 after SCI (Fig. 6b). The Feb-1 + MSCs treatment regimen was higher than the SCI group not only in Catwalk step sequence analysis scores but also in print width scores (Figs. 6c and 7d, e).

The Feb-1 + MSCs + NPs treatment regimen had significantly higher BBB scores than the Feb-1 alone regimen starting at week five and higher than the Feb-1 + MSCs treatment regimen at week six (Fig. 6b). In addition, the Feb-1 + MSCs + NPs treatment regimen was significantly higher than the SCI group in several Catwalk analysis measures such as step sequence, print area, print length, print width, and swing speed (Fig. 6c–e, 7a-g).

The experiment used motor-evoked potentials to assess neurological recovery. The results suggested that the peak-to-peak amplitude of Feb-1 + MSCs and Feb-1+MSCs+NPs group was higher than that of the SCI group. In addition, the amplitude of the Feb-1+MSCs+NPs group was significantly higher than that of the SCI group, the Feb-1 group, and the Feb-1+MSCs group, displaying a well-recovered nerve conduction function (Fig. 7h and i).

Finally, all rats were sacrificed at the sixth week of the experiment, and neuronal cells and astrocytes were labeled using immunofluorescent staining (Fig. 6f). The results showed that Feb-1, Feb-1 + MSCs, and Feb-1 + MSCs + NPs treatment regimens all significantly reduced neuronal cell loss after SCI (Fig. 6i). What's more, Feb-1 + MSCs + NPs treatment regimen not only promotes neuronal cell survival after SCI but also reduces the size of the cavity after SCI (Fig. 6j). Collectively, our research affirms that the treatment combination of Feb-1, MSCs, and NPs produces beneficial therapeutic effects, promoting SCI repair and enhancing functional recovery in rats.

4. Discussion

Spinal cord injury inevitably leads to the accumulation of reactive oxygen species (ROS) and pro-inflammatory factors within the lesion microenvironment, contributing to further neuronal damage [59–61]. MSCs transplantation is currently a promising treatment for neurological diseases. MSCs can secrete various neurotrophic factors and anti-inflammatory cytokines to help the repair of SCI [62,63]. With the advancement of technology, biomaterials have received attention from researchers in promoting tissue repair and improving stem cell survival rates [64–66]. The incorporation of MSCs augmented with nanodrugs, engineered to support regeneration, save neurons, and provide neurotrophic benefits, represents a viable approach for SCI treatment [67].

For example, some researchers have attempted to use membranes or exosomes derived from MSCs for nanomedicine delivery. However, these strategies suffer from poor sustainability, involuted extraction process, and heterogeneity of vesicle populations [38,68]. It is also reported that genetic modification of MSCs is likely to exert therapeutic effects, while the safety concerns posed by GM technology still face difficulties [69]. With the development of biomaterials, biomaterials present a broad prospect in ROS scavenging, drug-targeted delivery, and inflammation modulation, providing new possibilities for SCI repair [70–73].

Recent reports indicate that a "cellular backpack" strategy is being used for the treatment of stroke, which conjugates drug-loaded micelles on the surface of MSCs. The results confirmed that packed MSCs showed excellent efficacy in cell migration, cell survival, and reduction of oxidative stress in the lesion area [74,75]. The nanodrug micelles conjugation strategies on the surface of MSCs have a crucial impact on vesicle release and further therapeutic efficacy. In this study, we have demonstrated that the Tz-A6 peptide, through its specific binding to CD44 positive MSCs, significantly promotes the internalization of the nanodrug in vitro. This finding aligns with outcomes documented in prior research [76].

In addition, many neuroprotective agents have excellent free radical scavenging abilities and can modulate the SCI microenvironment. What's more, this kind of drug also possesses a promising application in protecting the viability of MSCs. Challenges such as inadequate targeting and metabolic instability remain. For instance, Fer-1, a frequently used free radical scavenger, has an extremely short half-life in rats [48]. Many efforts were undertaken to enhance the efficacy of this molecule and also to improve the pharmacokinetic parameters of Fer-1 [77,78]. Here, we have developed a ROS-responsive anti-ferroptosis drug Feborastatin-1 (Feb-1) with a boronic ester group aimed to enhance the stability in vivo. Boronic ester is a relatively slow responsive masking group [49], which results in sustained release of the Feb-1 and reduces potential toxicity. Notably, ROS-responsive release was able to avoid off-target clearance of Feb-1.

Given all that, we have developed a methodology for the ROS nanoparticles that enables biomolecular CD44 labeling, bioconjugation of CD44-positive cell membranes with nanomedicine loading capacity, and transmembrane transportation when combined with a biorthogonal strategy. In the nanoparticles, Feb-1 was prepared as a protective agent, it showed remarkable anti-ferroptosis and antioxidative effects. Our findings affirm the biocompatibility of ROS Nano@Feb-1, its efficacy in lowering Huc-MSCs ROS levels, and its ability to inhibit cellular ferroptosis. Further in vivo and in vitro studies revealed that Feb-1 could achieve anti-ferroptosis by enhancing GPX-4 and xCT signaling pathways. Notably, Feb-1 contributes to functional recovery in rats with SCI. Besides, the combination of Feb-1, MSCs, and NPs produces beneficial therapeutic effects and promotes the repair and functional recovery of SCI in rats.

Ethics approval and consent to participate

All animal experiments have been approved by the Ethics Committee of Tianjin Medical University General Hospital (Tianjin, China; IRB2023-DW-114). All the animals from Beijing Vital River Laboratory Animal Technology Co., Ltd. We confirm that all authors comply with all relevant ethical regulations.

Declaration of competing interest

The authors declare that they have no known competing financial interests or personal relationships that could have appeared to influence the work reported in this paper.

CRediT authorship contribution statement

Renshuai Hua: Visualization, Project administration, Methodology, Formal analysis, Data curation. **Chenxi Zhao:** Resources, Investigation, Data curation. **Zhengyu Xu:** Validation, Software, Methodology. **Derong Liu:** Methodology. **Wenyuan Shen:** Validation. **Wenlu Yuan:** Supervision. **Yan Li:** Project administration. **Jun Ma:** Formal analysis. **Zhishuo Wang:** Writing – review & editing, Writing – original draft, Conceptualization. **Shiqing Feng:** Writing – review & editing, Writing – original draft, Supervision, Data curation, Conceptualization.

Acknowledgements

This work was supported by the National Key Research and Development Project of Stem Cell and Transformation Research (2019YFA0112100), Tianjin Key Medical Discipline (Specialty) Construct Project (TJYXZDXK-027A), International Innovation Summit for Academicians and Experts (22JRRCRC00010). We thank the Large Instrument Sharing Platform of Tianjin Medical University for the availability of the instruments.

Appendix A. Supplementary data

Supplementary data to this article can be found online at https://doi.org/10.1016/j.bioactmat.2024.05.015.

References

[1] GBD 2016 Neurology Collaborators, Global, regional, and national burden of neurological disorders, 1990-2016: a systematic analysis for the Global Burden of Disease Study 2016, Lancet Neurol. 18 (5) (2019) 459–480.

[2] J.H. Badhiwala, J.R. Wilson, C.D. Witiw, J.S. Harrop, A.R. Vaccaro, B. Aarabi, R. G. Grossman, F.H. Geisler, M.G. Fehlings, The influence of timing of surgical decompression for acute spinal cord injury: a pooled analysis of individual patient data, Lancet Neurol. 20 (2) (2021) 117–126.

[3] M.B. Bracken, M.J. Shepard, W.F. Collins, T.R. Holford, W. Young, D.S. Baskin, H. M. Eisenberg, E. Flamm, L. Leo-Summers, J. Maroon, A randomized, controlled trial of methylprednisolone or naloxone in the treatment of acute spinal-cord injury. Results of the Second National Acute Spinal Cord Injury Study, N. Engl. J. Med. 322 (20) (1990) 1405–1411.

[4] T.H. Hutson, S. Di Giovanni, The translational landscape in spinal cord injury: focus on neuroplasticity and regeneration, Nat. Rev. Neurol. 15 (12) (2019) 732–745.

[5] T. Ma, J. Wu, J. Mu, J. Gao, Biomaterials reinforced MSCs transplantation for spinal cord injury repair, Asian J. Pharm. Sci. 17 (1) (2022) 4–19.

[6] F. Rossi, G. Perale, S. Papa, G. Forloni, P. Veglianese, Current options for drug delivery to the spinal cord, Expet Opin. Drug Deliv. 10 (3) (2013) 385–396.

[7] I. Vismara, S. Papa, F. Rossi, G. Forloni, P. Veglianese, Current options for cell therapy in spinal cord injury, Trends Mol. Med. 23 (9) (2017) 831–849.

[8] T.B. Ribeiro, A.S.S. Duarte, A.L.F. Longhini, F. Pradella, A.S. Farias, A.C.M. Luzo, A. L.R. Oliveira, S.T. Olalla, Saad Neuroprotection and immunomodulation by xenografted human mesenchymal stem cells following spinal cord ventral root avulsion, Sci. Rep. 5 (2015) 16167.

[9] J. Deng, M. Li, F. Meng, Z. Liu, S. Wang, Y. Zhang, M. Li, Z. Li, L. Zhang, P. Tang, 3D spheroids of human placenta-derived mesenchymal stem cells attenuate spinal cord injury in mice, Cell Death Dis. 12 (12) (2021) 1096.

[10] C.P. Hofstetter, E.J. Schwarz, D. Hess, J. Widenfalk, A. El Manira, D.J. Prockop, L. Olson, Marrow stromal cells form guiding strands in the injured spinal cord and promote recovery, Proc. Natl. Acad. Sci. U.S.A. 99 (4) (2002) 2199–2204.

[11] J.L. Markman, A. Rekechenetskiy, E. Holler, J.Y. Ljubimova, Nanomedicine therapeutic approaches to overcome cancer drug resistance, Adv. Drug Deliv. Rev. 65 (13–14) (2013) 1866–1879.

[12] A. Zarepour, A.B. Öztürk, D.K. Irmak, G. Yaşayan, A. Gökmen, E. Karaöz, A. Zarepour, A. Zarrabi, E. Mostafavi, Biopharmaceutics Combination Therapy Using Nanomaterials and Stem Cells to Treat Spinal Cord Injuries, Eur. J. Pharm. Biopharm. 177 (2022) 224–240.

[13] J. Zeng, C. Gu, Y. Sun, X. Chen, Engineering of M2 Macrophages-Derived Exosomes via Click Chemistry for Spinal Cord Injury Repair, Adv. Healthcare Mater. 12 (11) (2023) 2203391.

[14] C. Pan, X. Jiang, C. Liu, J. Wei, Y. Wang, C. Yang, Y. Gan, Bioorthogonal chemistry mediated cell engineering for advanced cell and cell-derived vesicle therapies: principles, progresses, and remaining challenges, Chem. Eng. J. 480 (2024) 148120.

[15] Y. Rong, Z. Wang, P. Tang, J. Wang, C. Ji, J. Chang, Y. Zhu, W. Ye, J. Bai, W. Liu, G. Yin, L. Yu, X. Zhou, W. Cai, Engineered extracellular vesicles for delivery of siRNA promoting targeted repair of traumatic spinal cord injury, Bioact. Mater. 23 (2023) 328–342.

[16] H.-H. Wu, Y. Zhou, Y. Tabata, J.-Q. Gao, Mesenchymal stem cell-based drug delivery strategy: from cells to biomimetic, J. Contr. Release 294 (2019) 102–113.

[17] P. Bonilla, J. Hernandez, E. Giraldo, M.A. González-Pérez, A. Alastrue-Agudo, H. Elkhenany, M.J. Vicent, X. Navarro, M. Edel, V. Moreno-Manzano, Human-induced neural and mesenchymal stem cell therapy combined with a curcumin nanoconjugate as a spinal cord injury treatment, Int. J. Mol. Sci. 22 (11) (2021) 5966.

[18] O.I. Eseonu, C. De, Bari Homing of mesenchymal stem cells: mechanistic or stochastic? Implications for targeted delivery in arthritis, Rheumatology 54 (2) (2015) 210–218.

[19] J.M. Ryan, F.P. Barry, J.M. Murphy, B.P. Mahon, Mesenchymal stem cells avoid allogeneic rejection, J. Inflamm. 2 (2005) 8.

[20] I. Caron, F. Rossi, S. Papa, R. Aloe, M. Sculco, E. Mauri, A. Sacchetti, E. Erba, N. Panini, V. Parazzi, M. Barilani, G. Forloni, G. Perale, L. Lazzari, P. Veglianese, A new three dimensional biomimetic hydrogel to deliver factors secreted by human mesenchymal stem cells in spinal cord injury, Biomaterials 75 (2016) 135–147.

[21] Y. Jin, Z. Tang, S. Shang, Y. Chen, G. Han, M. Song, J. Zhou, H. Zhang, Y. Ding, A nanodisc-paved biobridge facilitates stem cell membrane fusogenicity for intracerebral shuttling and bystander effects, Adv. Mater. 35 (40) (2023) e2302367.

[22] Y. Li, Z. Zhong, C. Xu, X. Wu, J. Li, W. Tao, J. Wang, Y. Du, S. Zhang, 3D micropattern force triggers YAP nuclear entry by transport across nuclear pores and modulates stem cells paracrine, Natl. Sci. Rev. 10 (8) (2023) nwad165.

[23] H. Zhou, Y. He, W. Xiong, S. Jing, X. Duan, Z. Huang, G.S. Nahal, Y. Peng, M. Li, Y. Zhu, Q. Ye, MSC based gene delivery methods and strategies improve the therapeutic efficacy of neurological diseases, Bioact. Mater. 23 (2023) 409–437.

[24] X. Yao, Y. Zhang, J. Hao, H.-Q. Duan, C.-X. Zhao, C. Sun, B. Li, B.-Y. Fan, X. Wang, W.-X. Li, X.-H. Fu, Y. Hu, C. Liu, X.-H. Kong, S.-Q. Feng, Deferoxamine promotes recovery of traumatic spinal cord injury by inhibiting ferroptosis, Neural Regen Res 14 (3) (2019) 532–541.

[25] L. Guha, N. Singh, H. Kumar, Different ways to die: cell death pathways and their association with spinal cord injury, Neurospine 20 (2) (2023) 430–448.

[26] W. Li, X. Zhao, R. Zhang, X. Liu, Z. Qi, Y. Zhang, W. Yang, Y. Pang, C. Zhao, B. Fan, N. Ran, J. Zhang, X. Kong, S. Feng, X. Yao, Ferroptosis inhibition protects vascular endothelial cells and maintains integrity of the blood-spinal cord barrier after spinal cord injury, Neural Regen Res 18 (11) (2023) 2474–2481.

[27] X.-Y. Bai, X.-L. Liu, Z.-Z. Deng, D.-M. Wei, D. Zhang, H.-L. Xi, Q.-Y. Wang, M.-Z. He, Y.-L. Yang, Ferroptosis is a new therapeutic target for spinal cord injury, Front. Neurosci. 17 (2023) 1136143.

[28] S. Li, C. Zhou, Y. Zhu, Z. Chao, Z. Sheng, Y. Zhang, Y. Zhao, Ferrostatin-1 alleviates angiotensin II (Ang II)- induced inflammation and ferroptosis in astrocytes, Int. Immunopharm. 90 (2021) 107179.

[29] J. Chu, C.-X. Liu, R. Song, Q.-L. Li, Ferrostatin-1 protects HT-22 cells from oxidative toxicity, Neural Regen Res 15 (3) (2020) 528–536.

[30] S. Hofmans, T. Vanden Berghe, L. Devisscher, B. Hassannia, S. Lyssens, J. Joossens, P. Van Der Veken, P. Vandenabeele, K. Augustyns, Novel ferroptosis inhibitors with improved potency and ADME properties, J. Med. Chem. 59 (5) (2016) 2041–2053.

[31] P. Zhou, X. Zhang, X. Xin, J. Yang, Q. Pan, C. Liu, Y. Liu, X. Yu, Z. Li, G. Jiao, X. Liu, Click chemistry-conjugated protein-drug micelles with anti-ferroptotic and anti-inflammatory properties promote regeneration in spinal cord injury, Chem. Eng. J. 428 (2022) 132118.

[32] C. Fu, X. Mao, X. Jin, T. Zuo, M. Zheng, J. Wang, Y. Fan, L. Xu, J. Lou, D. Shi, Magnetotactic bacteria-derived Mms6 gene helps M2 macrophages to form magnetic bio-nanoparticles to prevent ferroptosis and promote locomotor functional recovery after spinal cord injury in mice, Adv. Funct. Mater. 33 (51) (2023) 2305325.

[33] Z. Zhang, Q. Wang, Q. Liu, Y. Zheng, C. Zheng, K. Yi, Y. Zhao, Y. Gu, Y. Wang, C. Wang, X. Zhao, L. Shi, C. Kang, Y. Liu Dual-Locking, Nanoparticles disrupt the PD-1/PD-L1 pathway for efficient cancer immunotherapy, Adv. Mater. 31 (51) (2019) e1905751.

[34] Y. Zuo, J. Ye, W. Cai, B. Guo, X. Chen, L. Lin, S. Jin, H. Zheng, A. Fang, X. Qian, Z. Abdelrahman, Z. Wang, Z. Zhang, Z. Chen, B. Yu, X. Gu, X. Wang, Controlled delivery of a neurotransmitter-agonist conjugate for functional recovery after severe spinal cord injury, Nat. Nanotechnol. 18 (10) (2023) 1230–1240.

[35] M. Dominici, K. Le Blanc, I. Mueller, I. Slaper-Cortenbach, F. Marini, D. Krause, R. Deans, A. Keating, D. Prockop, E. Horwitz, Minimal criteria for defining multipotent mesenchymal stromal cells. The International Society for Cellular Therapy position statement, Cytotherapy 8 (4) (2006) 315–317.

[36] D.M. Basso, M.S. Beattie, J.C. Bresnahan, A sensitive and reliable locomotor rating scale for open field testing in rats, J. Neurotrauma 12 (1) (1995) 1–21.

[37] K.L. Kozielski, A. Jahanshahi, H.B. Gilbert, Y. Yu, Ö. Erin, D. Francisco, F. Alosaimi, Y. Temel, M. Sitti, Nonresonant powering of injectable nanoelectrodes enables wireless deep brain stimulation in freely moving mice, Sci. Adv. 7 (3) (2021) eabc4189.

[38] N. Ran, W. Li, R. Zhang, C. Lin, J. Zhang, Z. Wei, Z. Li, Z. Yuan, M. Wang, B. Fan, W. Shen, X. Li, H. Zhou, X. Yao, X. Kong, S. Feng, Autologous exosome facilitates load and target delivery of bioactive peptides to repair spinal cord injury, Bioact. Mater. 25 (2023) 766–782.

[39] C. Zhang, D. Guo, H. Qiao, J. Li, J. Li, Y. Yang, S.e. Chang, F. Li, D. Wang, H. Li, X. He, F. Wang, Macrophage extracellular traps exacerbate secondary spinal cord injury by modulating macrophage/microglia polarization via LL37/P2X7R/NF-κB signaling pathway, Oxid. Med. Cell. Longev. 2022 (2022) 9197940.

[40] E.J.L. Stéen, J.T. Jørgensen, K. Johann, K. Nørregaard, B. Sohr, D. Svatunek, A. Birke, V. Shalgunov, P.E. Edem, R. Rossin, C. Seidl, F. Schmid, M.S. Robillard, J. L. Kristensen, H. Mikula, M. Barz, A. Kjær, M.M. Herth, Trans-cyclooctene-functionalized PeptoBrushes with improved reaction kinetics of the tetrazine ligation for pretargeted nuclear imaging, ACS Nano 14 (1) (2020) 568–584.

[41] G. Lu, F. Li, F. Zhang, L.L. Huang, L. Zhang, Y. Lv, W. Wei, H.Y. Xie, Amplifying nanoparticle targeting performance to tumor via diels–alder cycloaddition, Adv. Funct. Mater. 28 (30) (2018) 1707596.

[42] X. Wu, Y. Zhang, K. Takle, O. Bilsel, Z. Li, H. Lee, Z. Zhang, D. Li, W. Fan, C. Duan, E.M. Chan, C. Lois, Y. Xiang, G. Han, Dye-sensitized core/active shell upconversion nanoparticles for optogenetics and bioimaging applications, ACS Nano 10 (1) (2016) 1060–1066.

[43] C.J. Martínez Rivas, M. Tarhini, W. Badri, K. Miladi, H. Greige-Gerges, Q.A. Nazari, S.A. Galindo Rodríguez, R.Á. Román, H. Fessi, A. Elaissari Nanoprecipitation process: from encapsulation to drug delivery, Int. J. Pharm. 532 (1) (2017) 66–81.

[44] L. Lin, H. Gong, R. Li, J. Huang, M. Cai, T. Lan, W. Huang, Y. Guo, Z. Zhou, Y. An, Z. Chen, L. Liang, Y. Wang, X. Shuai, K. Zhu, Nanodrug with ROS and pH dual-sensitivity ameliorates liver fibrosis via multicellular regulation, Adv. Sci. 7 (7) (2020) 1903138.

[45] Y. Lu, Z. Guo, Y. Zhang, C. Li, Y. Zhang, Q. Guo, Q. Chen, X. Chen, X. He, L. Liu, C. Ruan, T. Sun, B. Ji, W. Lu, C. Jiang, Microenvironment remodeling micelles for alzheimer's disease therapy by early modulation of activated microglia, Adv. Sci. 6 (4) (2019) 1801586.

[46] W. Gu, T. Liu, D. Fan, J. Zhang, Y. Xia, F. Meng, Y. Xu, J.J.L.M. Cornelissen, Z. Liu, Z. Zhong, A6 peptide-tagged, ultra-small and reduction-sensitive polymersomal vincristine sulfate as a smart and specific treatment for CD44+ acute myeloid leukemia, J. Contr. Release 329 (2021) 706–716.

[47] W. Gu, J. An, H. Meng, N. Yu, Y. Zhong, F. Meng, Y. Xu, J.J.L.M. Cornelissen, Z. Zhong, CD44-Specific A6 short peptide boosts targetability and anticancer efficacy of polymersomal epirubicin to orthotopic human multiple myeloma, Adv. Mater. 31 (46) (2019) e1904742.

[48] L. Devisscher, S. Van Coillie, S. Hofmans, D. Van Rompaey, K. Goossens, E. Meul, L. Maes, H. De Winter, P. Van Der Veken, P. Vandenabeele, T.V. Berghe, K. Augustyns Discovery of Novel, Drug-like ferroptosis inhibitors with in vivo efficacy, J. Med. Chem. 61 (22) (2018) 10126–10140.
[49] M. Liu, Y. Luo, J. Yan, X. Xiong, X. Xing, J.S. Kim, T. Zou, Photoactivation of boronic acid prodrugs via a phenyl radical mechanism: iridium(III) anticancer complex as an example, J. Am. Chem. Soc. 145 (18) (2023) 10082–10091.
[50] J. Wu, R. Xue, M. Wu, X. Yin, B. Xie, Q. Meng, Nrf2-Mediated ferroptosis inhibition exerts a protective effect on acute-on-chronic liver failure, Oxid. Med. Cell. Longev. 2022 (2022) 4505513.
[51] S.J. Dixon, K.M. Lemberg, M.R. Lamprecht, R. Skouta, E.M. Zaitsev, C.E. Gleason, D.N. Patel, A.J. Bauer, A.M. Cantley, W.S. Yang, B. Morrison, B.R. Stockwell, Ferroptosis: an iron-dependent form of nonapoptotic cell death, Cell 149 (5) (2012) 1060–1072.
[52] I. Ingold, C. Berndt, S. Schmitt, S. Doll, G. Poschmann, K. Buday, A. Roveri, X. Peng, F. Porto Freitas, T. Seibt, L. Mehr, M. Aichler, A. Walch, D. Lamp, M. Jastroch, S. Miyamoto, W. Wurst, F. Ursini, E.S.J. Arnér, N. Fradejas-Villar, U. Schweizer, H. Zischka, J.P. Friedmann Angeli, M. Conrad, Selenium utilization by GPX4 is required to prevent hydroperoxide-induced ferroptosis, Cell 172 (3) (2018) 409–422.
[53] H. Imai, M. Matsuoka, T. Kumagai, T. Sakamoto, T. Koumura, Lipid peroxidation-dependent cell death regulated by GPx4 and ferroptosis, Curr. Top. Microbiol. Immunol. 403 (2017) 143–170.
[54] M.-M. Han, X.-Y. He, L. Tang, L. Qi, M.-Y. Yang, Y. Wang, L. Xing, J.-H. Jeong, H.-L. Jiang, Nanoengineered mesenchymal stem cell therapy for pulmonary fibrosis in young and aged mice, Sci. Adv. 9 (29) (2023) eadg5358.
[55] B. Fan, Z. Wei, X. Yao, G. Shi, X. Cheng, X. Zhou, H. Zhou, G. Ning, X. Kong, S. Feng, Microenvironment imbalance of spinal cord injury, Cell Transplant. 27 (6) (2018) 853–866.
[56] Z. Zhou, X. Tian, B. Mo, H. Xu, L. Zhang, L. Huang, S. Yao, Z. Huang, Y. Wang, H. Xie, L. Xu, H. Zhang, Adipose mesenchymal stem cell transplantation alleviates spinal cord injury-induced neuroinflammation partly by suppressing the Jagged1/Notch pathway, Stem Cell Res. Ther. 11 (1) (2020) 212.
[57] Q.-M. Pang, S.-Y. Chen, Q.-J. Xu, S.-P. Fu, Y.-C. Yang, W.-H. Zou, M. Zhang, J. Liu, W.-H. Wan, J.-C. Peng, T. Zhang Neuroinflammation, Scarring after spinal cord injury: therapeutic roles of MSCs on inflammation and glial scar, Front. Immunol. 12 (2021) 751021.
[58] P. Liu, Y. Feng, H. Li, X. Chen, G. Wang, S. Xu, Y. Li, L. Zhao, Ferrostatin-1 alleviates lipopolysaccharide-induced acute lung injury via inhibiting ferroptosis, Cell. Mol. Biol. Lett. 25 (2020) 1–14.
[59] H. Wang, F. Lin, Y. Wu, W. Guo, X. Chen, C. Xiao, M. Chen, Carrier-free nanodrug based on Co-assembly of methylprednisolone dimer and rutin for combined treatment of spinal cord injury, ACS Nano 17 (13) (2023) 12176–12187.
[60] Y. Yang, Z. Huang, Y. Tu, Q. Wu, Z. Li, Y. Zhang, H. Yu, A. Zeng, H. Huang, J. Ye, W. Ying, M. Chen, Z. Feng, Z. Xiang, Q. Ye, S. Zhu, Z. Wang, A shear-thinning, ROS-scavenging hydrogel combined with dental pulp stem cells promotes spinal cord repair by inhibiting ferroptosis, Bioact. Mater. 22 (2023) 274–290.
[61] Z. Li, T. Zhao, J. Ding, H. Gu, Q. Wang, Y. Wang, D. Zhang, C. Gao, A reactive oxygen species-responsive hydrogel encapsulated with bone marrow derived stem cells promotes repair and regeneration of spinal cord injury, Bioact. Mater. 19 (2023) 550–568.
[62] M. Boido, A. Piras, V. Valsecchi, G. Spigolon, K. Mareschi, I. Ferrero, A. Vizzini, S. Temi, L. Mazzini, F. Fagioli, A. Vercelli Human mesenchymal stromal cell transplantation modulates neuroinflammatory milieu in a mouse model of amyotrophic lateral sclerosis, Cytotherapy 16 (8) (2014) 1059–1072.
[63] Z. Zhang, F. Wang, M. Song, The cell repair research of spinal cord injury: a review of cell transplantation to treat spinal cord injury, J. Neurorestoratology 7 (2) (2019) 55–62.
[64] D. Zhu, Y. Su, M.L. Young, J. Ma, Y. Zheng, L. Tang, Biological responses and mechanisms of human bone marrow mesenchymal stem cells to Zn and Mg biomaterials, ACS Appl. Mater. Interfaces 9 (33) (2017) 27453–27461.
[65] W. Jiang, A.F. Cipriano, Q. Tian, C. Zhang, M. Lopez, A. Sallee, A. Lin, M.C. Cortez Alcaraz, Y. Wu, Y. Zheng, H. Liu, In vitro evaluation of MgSr and MgCaSr alloys via direct culture with bone marrow derived mesenchymal stem cells, Acta Biomater. 72 (2018) 407–423.
[66] Y. Han, Y. Wu, F. Wang, G. Li, J. Wang, X. Wu, A. Deng, X. Ren, X. Wang, J. Gao, Z. Shi, L. Bai, J. Su, Heterogeneous DNA hydrogel loaded with Apt02 modified tetrahedral framework nucleic acid accelerated critical-size bone defect repair, Bioact. Mater. 35 (2024) 1–16.
[67] E. García, S. Sánchez-Noriega, G. González-Pacheco, A.N. González-Vázquez, A. Ibarra, R. Rodríguez-Barrera, Recent advances in the combination of cellular therapy with stem cells and nanoparticles after a spinal cord injury, Front. Neurol. 14 (2023) 1127878.
[68] Z. Cao, P. Li, Y. Li, M. Zhang, M. Hao, W. Li, X. Mao, L. Mo, C. Yang, X. Ding, Y. Y. Yang, P. Yuan, S. Shi, X. Kou, Encapsulation of nano-bortezomib in apoptotic stem cell-derived vesicles for the treatment of multiple myeloma, Small 19 (40) (2023) e2301748.
[69] A. Andrzejewska, S. Dabrowska, B. Lukomska, M. Janowski Mesenchymal, Stem cells for neurological disorders, Adv. Sci. 8 (7) (2021) 2002944.
[70] Q. Zhang, W. Chen, G. Li, Z. Ma, M. Zhu, Q. Gao, K. Xu, X. Liu, W. Lu, W. Zhang, Y. Wu, Z. Shi, J. Su, A factor-free hydrogel with ROS scavenging and responsive degradation for enhanced diabetic bone healing, Small (2024) e2306389.
[71] J. Guo, F. Wang, Y. Hu, Y. Luo, Y. Wei, K. Xu, H. Zhang, H. Liu, L. Bo, S. Lv, S. Sheng, X. Zhuang, T. Zhang, C. Xu, X. Chen, J. Su, Exosome-based bone-targeting drug delivery alleviates impaired osteoblastic bone formation and bone loss in inflammatory bowel diseases, Cell Rep Med 4 (1) (2023) 100881.
[72] D. Liu, G. Lu, B. Shi, H. Ni, J. Wang, Y. Qiu, L. Yang, Z. Zhu, X. Yi, X. Du, B. Shi, ROS-scavenging hydrogels synergize with neural stem cells to enhance spinal cord injury repair via regulating microenvironment and facilitating nerve regeneration, Adv. Healthcare Mater. 12 (18) (2023) e2300123.
[73] S. Papa, I. Caron, E. Erba, N. Panini, M. De Paola, A. Mariani, C. Colombo, R. Ferrari, D. Pozzer, E.R. Zanier, F. Pischiutta, J. Lucchetti, A. Bassi, G. Valentini, G. Simonutti, F. Rossi, D. Moscatelli, G. Forloni, P. Veglianese, Early modulation of pro-inflammatory microglia by minocycline loaded nanoparticles confers long lasting protection after spinal cord injury, Biomaterials 75 (2016) 13–24.
[74] N. Kapate, M. Dunne, N. Kumbhojkar, S. Prakash, L.L.-W. Wang, A. Graveline, K. S. Park, V. Chandran Suja, J. Goyal, J.R. Clegg, S. Mitragotri, A backpack-based myeloid cell therapy for multiple sclerosis, Proc. Natl. Acad. Sci. U.S.A. 120 (17) (2023) e2221535120.
[75] Y. You, Y. Liu, C. Ma, J. Xu, L. Xie, S. Tong, Y. Sun, F. Ma, Y. Huang, J. Liu, W. Xiao, C. Dai, S. Li, J. Lei, Q. Mei, X. Gao, J. Chen, Surface-tethered ROS-responsive micelle backpacks for boosting mesenchymal stem cell vitality and modulating inflammation in ischemic stroke treatment, J. Contr. Release 362 (2023) 210–224.
[76] B. Guo, J. Wei, J. Wang, Y. Sun, J. Yuan, Z. Zhong, F. Meng, CD44-targeting hydrophobic phosphorylated gemcitabine prodrug nanotherapeutics augment lung cancer therapy, Acta Biomater. 145 (2022) 200–209.
[77] L.A. Farmer, Z. Wu, J.-F. Poon, O. Zilka, S.M. Lorenz, S. Huehn, B. Proneth, M. Conrad, D.A. Pratt, Intrinsic and extrinsic limitations to the design and optimization of inhibitors of lipid peroxidation and associated cell death, J. Am. Chem. Soc. 144 (32) (2022) 14706–14721.
[78] J.P. Morrow, Z.A.I. Mazrad, A.I. Bush, K. Kempe, Poly(2-oxazoline) - ferrostatin-1 drug conjugates inhibit ferroptotic cell death, J. Contr. Release 350 (2022) 193–203.